FINAL REPORT

Development and Evaluation of an Airborne Superconducting Quantum Interference Device-Based Magnetic Gradiometer Tensor System for Detection, Characterization and Mapping of Unexploded Ordnance
SERDP Project MM-1316

AUGUST 2008

Dr. T. Jeffrey Gamey
Battelle, Oak Ridge Operations

This document has been approved for public release.

SERDP

DoD EPA DOE

Strategic Environmental Research and
Development Program

Report Documentation Page

Public reporting burden for the collection of information is estimated to average 1 hour per response, including the time for reviewing instructions, searching existing data sources, gathering and maintaining the data needed, and completing and reviewing the collection of information. Send comments regarding this burden estimate or any other aspect of this collection of information, including suggestions for reducing this burden, to Washington Headquarters Services, Directorate for Information Operations and Reports, 1215 Jefferson Davis Highway, Suite 1204, Arlington VA 22202-4302. Respondents should be aware that notwithstanding any other provision of law, no person shall be subject to a penalty for failing to comply with a collection of information if it does not display a currently valid OMB control number.

1. REPORT DATE	2. REPORT TYPE	3. DATES COVERED
01 AUG 2008	**N/A**	**-**

4. TITLE AND SUBTITLE	5a. CONTRACT NUMBER
Development and Evaluation of an Airborne Superconducting Quantum Interference Device-Based Magnetic Gradiometer Tensor System for Detection, Characterization and Mapping of Unexploded Ordnance	5b. GRANT NUMBER
	5c. PROGRAM ELEMENT NUMBER

6. AUTHOR(S)	5d. PROJECT NUMBER
	5e. TASK NUMBER
	5f. WORK UNIT NUMBER

7. PERFORMING ORGANIZATION NAME(S) AND ADDRESS(ES)	8. PERFORMING ORGANIZATION REPORT NUMBER
Battelle, Oak Ridge Operations	

9. SPONSORING/MONITORING AGENCY NAME(S) AND ADDRESS(ES)	10. SPONSOR/MONITOR'S ACRONYM(S)
	11. SPONSOR/MONITOR'S REPORT NUMBER(S)

12. DISTRIBUTION/AVAILABILITY STATEMENT
Approved for public release, distribution unlimited

13. SUPPLEMENTARY NOTES
The original document contains color images.

14. ABSTRACT

15. SUBJECT TERMS

16. SECURITY CLASSIFICATION OF:			17. LIMITATION OF ABSTRACT	18. NUMBER OF PAGES	19a. NAME OF RESPONSIBLE PERSON
a. REPORT	b. ABSTRACT	c. THIS PAGE	**UU**	**54**	
unclassified	**unclassified**	**unclassified**			

This page intentionally left blank.

Table of Contents

List of Acronyms

ADC	Analog to Digital Converter
AT/HEAT	Anti-Tank/High Explosive AT
CSIRO	Commonwealth Scientific and Industrial Research Organization
CSS	Coastal Systems Station
DREA	Defence Research Establishment Atlantic
ERDC	Environmental Research and Development Center
ESTCP	Environmental Security Technology Certification Program
FLL	Flux-Locked Loop
GPS/DGPS	Differential/Global Positioning System
HNC	Hunstville Engineering Support Center
IMU	Inertial Measurement Unit
NAVEODTECHDIV	Naval Explosive Ordnance Technology Division
NCSL	Naval Coastal Systems Laboratory
ORNL	Oak Ridge National Laboratory
RF	Radio Frequency
SERDP	Security Environmental Research and Development Program
SNR	Signal to Noise Ratio
SQUID	Superconducting Quantum Interference Device
Tc/HTc/LTc	Critical Temperature/High Tc/Low Tc
USGS	United States Geologic Survey
UXO	Unexploded Ordnance

Table of Figures

Table of Tables

This page intentionally left blank.

Final Project Report

Development and Evaluation of an Airborne Superconducting Quantum Interference Device-Based Magnetic Gradiometer Tensor System for Detection, Characterization, and Mapping of Unexploded Ordnance

Acknowledgements

Executive Summary

The objective of this project was to develop and demonstrate an airborne full-tensor magnetic gradiometer for detection and precision mapping of UXO. The system was based on a liquid nitrogen-cooled high-temperature Superconducting QUantum Interference Device (SQUID) developed in a project funded by the U.S. Department of Energy and the U.S. Navy's Explosive Ordnance Disposal Technology Division. This SQUID sensor was to be integrated with the airborne geophysical platform originally deployed by Oak Ridge National Laboratory (ORNL)[1] and now by Battelle. This project included the design and testing of the SQUID sensor and characterization of the noise signatures in flight. Processing and analysis tools for the tensor data were developed to reduce or remove the noise signatures and to maximize the detection thresholds at large sensor-target offsets.

The high-temperature SQUID proved successful in stationary operation, for which it was originally designed. On a moving platform, numerous technical problems with the instrument arose, some of which could not be resolved or even explained. Continuous review of ongoing research in the field indicates that a low-temperature (liquid helium) intrinsic gradiometer system would be better suited to a moving platform despite the added complexity of a pressurized cryogenic vessel. Such a system is already in operation in a towed-bird helicopter, and stinger-mounted fixed-wing configuration. Its use as an electromagnetic receiver may also produce some benefit by virtue of operating in the system's lowest noise bandwidth.

---

[1] ORNL geophysical staff, equipment custody and project responsibility were relocated to Battelle in 2005.

Objective

Cost effective wide-area reconnaissance methods are needed to identify bombing targets and other unexploded ordnance (UXO)-laden areas that occur within larger uncharacterized areas. Airborne geophysical surveys can accomplish this goal at some sites, as demonstrated by the September 2007 Environmental Security Technology Certification Program (ESTCP) helicopter magnetometer demonstration at the Kirtland Air Force Base, New Mexico. The success at sites like Kirtland cannot be achieved, however, at all sites where UXO characterization is required, because stand-off distance is too great between the sensors and the ordnance objectives caused by vegetation or terrain; small ordnance items are below the detection threshold of current cesium vapor magnetometers; or other detrimental effects such as background geology raise the noise floor or reduce target signal strength. The increasing availability of robust SQUID technologies offers an opportunity to develop airborne sensors that have both increased resolution, and vector analysis capabilities. Such capabilities would open up more areas to wide-area assessment at lower cost.

The discovery of high temperature (HTc, liquid nitrogen) superconductivity in 1986 greatly expanded the potential for the use of superconducting quantum interference device (SQUID) sensors in field geophysics. These devices can be used either as magnetic or electromagnetic sensors and offer significantly greater sensitivity than either atomic magnetometers or induction coil receivers. They are also significantly less difficult to maintain than low temperature (LTc, liquid helium) SQUIDs, although at the cost of some sensitivity and considerably higher manufacturing prices.

As with a fluxgate magnetometer, each sensor measures flux in only one direction. Combinations of SQUID sensor elements are arranged in various configurations depending on the application requirements and the level of technical difficulty. As such, they have appeared as magnetic, magnetotelluric, gravimetric, frequency domain and time domain electromagnetic sensors; in borehole, ground, airborne and underwater platforms; and using from one to eight elements.

Although lower cost, higher quality, and higher resolution electronics have made high temperature SQUIDs more accessible, there are still design challenges which prevent their coming into common use. Their sensitivity makes them difficult to operate in unshielded environments. Their directional nature makes them sensitive to vibration and slight orientation changes. They have only recently (2004) been capable of intrinsic gradiometer configurations. The requirement for liquid nitrogen cooling makes them heavy to carry and difficult to maintain in the field. And higher manufacturing costs compared to mass-produced low temperature elements makes large arrays expensive to purchase and maintain.

Background

This section provides a brief overview of how a SQUID element works. A superconductor is a material which allows electrons to flow without any effective resistance. To date, this has only been possible within specific alloys at cryogenic temperatures. If the material is formed into a loop, changes in the magnetic flux through that loop will induce a current to flow. At a weak link, called a Josephson junction, the voltage across the gap can be measured. Rather than measuring the voltage directly, a high speed voltage regulator is applied to maintain a constant gap-voltage while the applied feedback voltage is measured instead (Figure 1). This is referred to as a flux-locked loop (FLL). Note that the FLL feedback responds only the *changes* in the magnetic field from its initial starting point, whatever that might be. SQUIDs therefore measure the relative magnetic field rather than the absolute field value the way that a fluxgate magnetometer would do. If the SQUID is shut down or loses lock, it has no way to relate the new readings to any previous readings.

The electronics of the FLL is capable of supplying only a limited range of feedback voltage. Once the FLL reaches its maximum capacity it must either flat-line or be reset to zero. In terms of the magnetic field flowing through the SQUID loop, this maximum voltage represents the limits of the dynamic range of the system. The FLL output needs to be converted from an analog to a digital signal for recording. This means that the dynamic range of the FLL voltage must be divided into bit-size units by the analog-to-digital converter (ADC). This determines the resolution of the output data. There is therefore a trade-off between the operational range of the system and the resolution of the output.
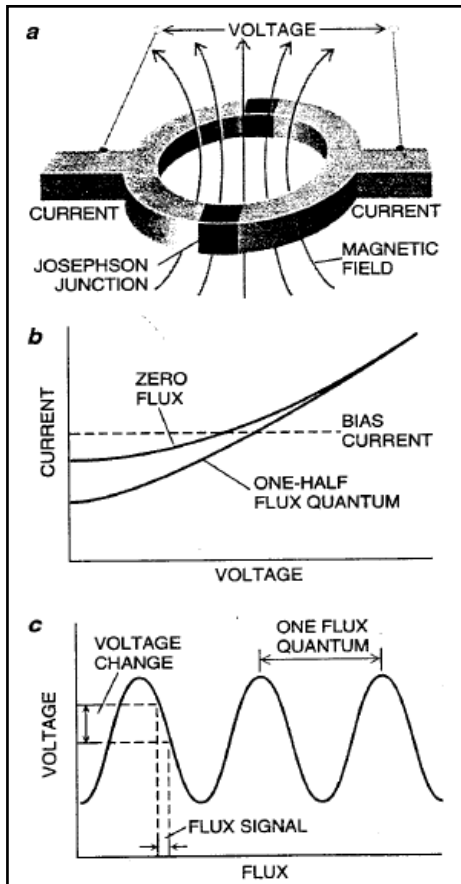
Figure 1: Basic functioning of a SQUID.
(a) The flux through the loop is measured as the voltage across a Josephson junction in a super-cooled conductor.
(b) A bias current is applied to lock the response on a single voltage.
(c) The voltage applied is directly related to the changes in flux through the loop. Its sensitivity arises from its ability to measure fractions of a quantum flux. (From Clarke, 1994).

SQUIDs are, by nature, sensitive instruments and are not particularly robust. Central to continuous operation is the ability of the FLL to maintain a lock on the signal. If the field change is so rapid that the FLL cannot keep up, the field is said to have exceeded the slew rate of the electronics. In this situation, several different outcomes are possible. If the loss of lock is temporary, the FLL will re-lock onto a different flux quantum. This is referred to as a cycle slip. It appears in the data as a DC offset in the data. Theoretically, these steps will be in multiples of flux quanta. Another possible outcome is that the sudden change in field traps flux within the SQUID. In this case the output response is no longer linked to changes in the field strength and the instrument appears to drift randomly until the trapped flux dissipates. The only reliable way to eliminate trapped flux is to re-heat the sensor element above the critical temperature (Tc) so that it no longer functions as a superconductor. After the element cools again, it is re-tuned (locked-on to a signal) and normal readings are again possible. This is ideally only required when the instrument is first initialized.

Simple SQUID elements measure the vector component of the external magnetic field. Assuming the external field is the Earth's field at 50,000nT, small changes in direction result in very large changes in SQUID response. A single vector system that is free to rotate in all directions must therefore have an effective dynamic range of +/-50,000nT. With the limitations of a 24-bit ADC, this reduces the resolution of the digital output to approximately 0.05nT. Steps must therefore be taken to limit the dynamic operating range of the system. An intrinsic gradiometer consists of a pair of counter-wound coaxial coils (Figure 2). This measures only the gradient field. A uniform field by definition has a gradient of zero, so intrinsic gradiometers need only be designed to handle the dynamic range of the expected anomalies – perhaps +/-500nT for the case of UXO. Unfortunately, alloys which become superconductors at relatively high liquid nitrogen temperatures (77K) are typically brittle and can only be formed into flat loops on circuit boards. Only low temperature superconducting materials (4K) can be formed into solid three-dimensional shapes. The exception to this is the HTc material developed by CSIRO in 2004, which can be laid onto a flexible substrate and curled over to form an intrinsic gradiometer. This technology is not yet commercially available.
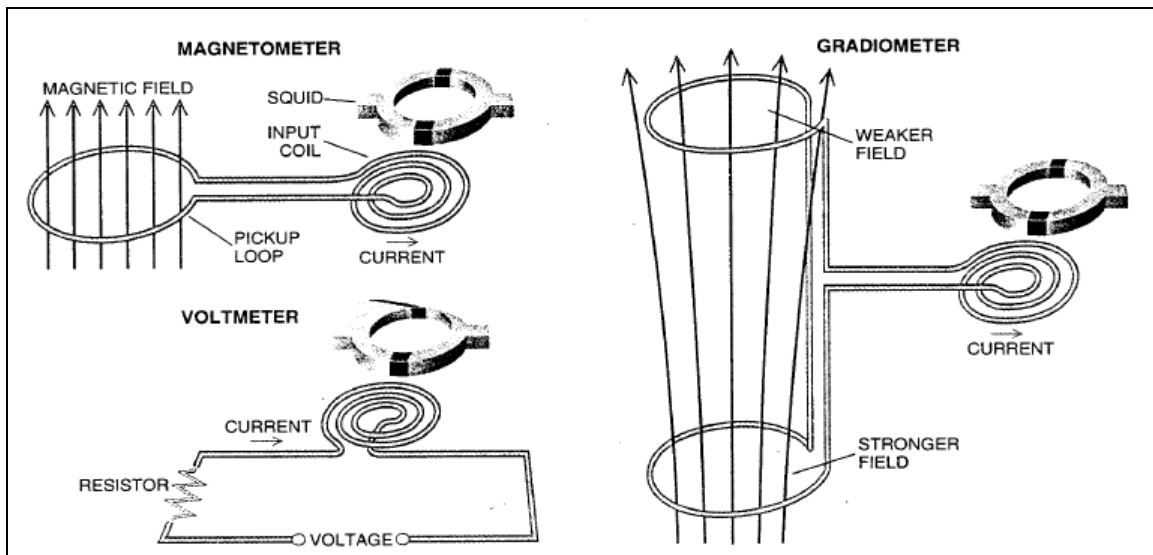
Figure 2: Demonstration of the difference between a single component total field magnetometer and intrinsic gradiometer. (From Clarke, 1994).

Materials and Methods

The objective of this project was to develop and demonstrate an airborne full-tensor magnetic gradiometer for detection and precision mapping of UXO. The system was based on a cryogenically-cooled Superconducting QUantum Interference Device (SQUID) developed in a project funded by the U.S. Department of Energy and the U.S. Navy's Explosive Ordnance Disposal Technology Division. This SQUID sensor was to be integrated with the airborne geophysical platform deployed by Battelle. This project included the design and testing of the SQUID sensor and characterization of the noise signatures in flight. Processing and analysis tools for the tensor data were developed to reduce or remove the noise signatures and to maximize the detection thresholds at large sensor-target offsets.

Initial stages of the project involved defining the nature of the various noise sources that would be encountered on an airborne platform. Electronics were designed around these expectations, and the resulting sensor package was tested for performance under conditions which simulated flight specifications. A man-portable platform was developed and tested over calibrated test grids.

The instrument in use for this project was a full tensor magnetic gradiometer provided to Battelle by the U.S. Navy to integrate into the existing airborne survey platform. It included eight SQUID elements in a single package that was immersed in a dewar of liquid nitrogen (Figure 3). The elements were arranged so as to measure all of the independent gradients of the total field components. Mathematical symmetry requires that only five of the nine possible gradients need to be measured in order to record the complete tensor matrix (
Figure **4**). Vector analysis of the tensor data allows equivalent dipole source locations to be determined for each reading, making it possible to track them in three dimensions.

Figure 3: Photos of the SQUID core and the dewar into which it is placed.

The technical approach began with developing suitable recording equipment capable of driving the SQUID instrument and handling the various noise sources that would be encountered in an airborne platform. Noise sources were broken down into the following subcategories. Each of these points is summarized in this report.

- Shielded operation (minimum noise floor)
- Unshielded operation (obtaining signal lock)
- Slew rate (limits of signal lock in dynamic environment)
- Physical vibration (boil-off, sloshing, physical damage)
- Aircraft compensation (low frequency signal)
- Rotor signal (high frequency signal)
- Geologic signal (wideband frequency signals)

Electronic design addressed each of these where appropriate. Other factors which could not be dealt with by engineering and signal processing, were dealt with by post-mission data processing procedures. Calibration for gain, orthogonality and linearity of the instruments were additional factors that are not unique to aircraft operations, but still had to be considered in the electronics design.

Additional shielding against RF interference was also required to allow stable operation in an unshielded environment. Physical vibration was dealt with through infrastructure solutions such as dewar design and shock absorbing mounting hardware. Software solutions were developed for the remaining issues. Where possible, these built on our direct experience with total field systems and the experience of others with vector systems. Data processing routines and inversion algorithms were developed in parallel with the instrument testing and were modified as new data became available.

$$
\begin{pmatrix} \dfrac{\partial H_x}{\partial x} & \dfrac{\partial H_x}{\partial z} \\[2ex] \dfrac{\partial H_y}{\partial x} & \dfrac{\partial H_y}{\partial z} \\[2ex] & \dfrac{\partial H_z}{\partial z} \end{pmatrix}
\Rightarrow
\begin{pmatrix} \dfrac{\partial H_x}{\partial x} & \dfrac{\partial H_x}{\partial y} & \dfrac{\partial H_x}{\partial z} \\[2ex] \dfrac{\partial H_y}{\partial x} & \dfrac{\partial H_y}{\partial y} & \dfrac{\partial H_y}{\partial z} \\[2ex] \dfrac{\partial H_z}{\partial x} & \dfrac{\partial H_z}{\partial y} & \dfrac{\partial H_z}{\partial z} \end{pmatrix}
$$
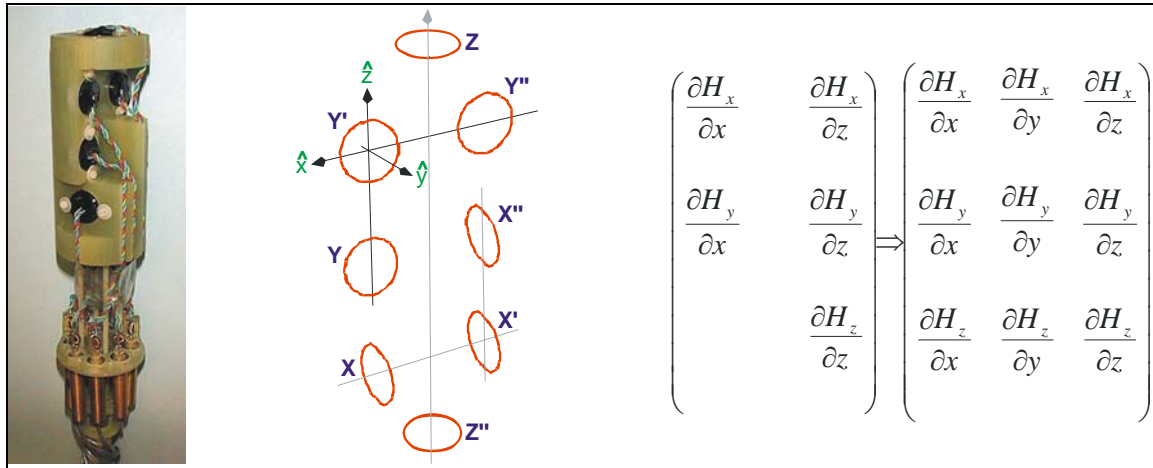
Figure 4: Close up photo of SQUID elements on the core, schematic of the vector orientations for each of the SQUID elements, and tensor matrix of component gradients. Only eight individual elements are required to measure the five gradients which completely define the tensor matrix.

<div align="center">**Results and Accomplishments**</div>

Electronics Design

The electronics design phase was intended to ensure that the hardware specifications were adequate to record the data with the necessary precision and resolution. The noise specifications were the primary drivers for these criteria, although there were certain aspects of the system where the electronics set the noise levels. The final design consisted of the SQUID and dewar controlled by the FLL electronics, with a dedicated recording console and user interface. The recording console also recorded a fluxgate magnetometer and the GPS information.   The recording system was designed to operate at a variety of user selectable output sample rates below 1200Hz. If required, two selected channels could be recorded at 10kHz.

The FLL electronics had a voltage range of +/-8V and the linearity of the response over this range was found to be good. The system was designed with three possible gain settings: 2000nT, 500nT and 100nT. These represented the limits of the operational dynamic range of the SQUID elements. When the response from any given element exceeded this limit, the system would reset to zero and continue recording. These reset events were recorded so that the full dynamic range of the original field could be reconstructed (Figure 5).
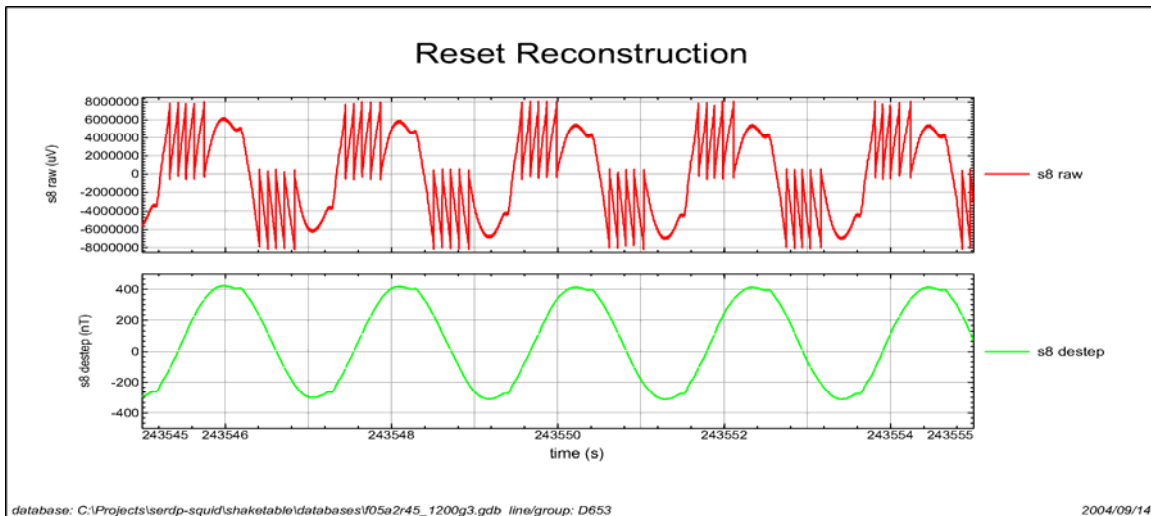
Figure 5: Sample of raw "saw-tooth" signal and reconstruction of the total field response.

This approach allowed the SQUID to function over an unlimited dynamic range while maintaining a high resolution. There were, however, limitations. The reset event was seen in the electronics as a high frequency event. The output of the ADC therefore exhibited ringing at each event and several data points on either side of the reset were lost. This meant that resets could not occur too close together or else there would be no valid (non-interpolated) data remaining. Gradient calculations were doubly susceptible to this, since data lost in either channel would be lost in the gradient. Tensor data was similarly hampered.

Another problem was the data reconstruction. Theoretically, the first value after a reset would be zero, plus or minus one flux quantum. This level of predictability was never observed in actual operation and an average value had to be used. This degraded the accuracy of the output with each successive reset. For both of these reasons, it was important to minimize the number of resets that would occur during any data collection.

<div align="center">7</div>

Shielded Operation

In July 2003, the SQUID sensor was mounted in a mu-metal shield at Tristan's facilities in San Diego to block the majority of the external magnetic and electromagnetic field. Sensor readings were made, including power spectrum plots, to determine the baseline performance of the sensor in an ideal setting. This formed the basis for all future comparisons and is ultimate noise floor of the instrument. A small access port was available through the base of the shield to pass small metallic targets. By dragging targets through this access port a profile of the response was measured. By moving the sensor within the shield and repeating the process, multiple profiles and (subsequently) a grid were produced. This was compared to theoretical models to verify the proper operation of the device.

Noise levels from the manufacturer indicated that the minimum noise floor for the instrument under perfect conditions was approximately 0.10 pT/√Hz at 1Hz and 0.062 pT/√Hz at 10Hz. This was the range of frequencies of greatest interest to low altitude helicopter surveys. At nominal airborne speeds and altitudes, a near-surface magnetic anomaly has a total field spectral peak in Hz at (speed / (6 x altitude)) and a vertical gradient spectral peak at (speed / (3 x altitude)). For the range of speeds (20-40 m/s) and altitudes (1-10m) anticipated, the bandwidth of particular interest is 0.1-10Hz. This is on the trailing edge of the 1/f noise range of the SQUID technology, which only reaches a stable noise floor above 10Hz. Noise levels at the 1Hz and 10Hz points are shown for each of the SQUID elements in Table 1. Average noise values range from 14pT at 1Hz down to 5pT at 10Hz.

Table 1: Shielded noise levels at 1 and 10Hz

	Tristan test		Manufacturer test	
Element	1 Hz	10 Hz	1 Hz	10 Hz
1	13.3 pT/√Hz	4.5 pT/√Hz	0.20 pT/√Hz	0.090 pT/√Hz
2	9.4 pT/√Hz	2.7 pT/√Hz	0.10 pT/√Hz	0.075 pT/√Hz
3	17.5 pT/√Hz	5.0 pT/√Hz	0.10 pT/√Hz	0.080 pT/√Hz
4	8.5 pT/√Hz	3.5 pT/√Hz	0.13 pT/√Hz	0.060 pT/√Hz
5	10.4 pT/√Hz	3.3 pT/√Hz	0.07 pT/√Hz	0.045 pT/√Hz
6	7.6 pT/√Hz	2.8 pT/√Hz	0.07 pT/√Hz	0.045 pT/√Hz
7	20.6 pT/√Hz	3.7 pT/√Hz	0.08 pT/√Hz	0.050 pT/√Hz
8	25.3 pT/√Hz	12.1 pT/√Hz	0.08 pT/√Hz	0.050 pT/√Hz
average	14.1 pT/√Hz	4.7 pT/√Hz	0.10 pT/√Hz	0.062 pT/√Hz

Additional tests included dragging targets beneath the SQUID inside the shield. Targets included a locator loop (a 20mm loop of wire encased in plastic with a regulated DC current flowing through it), and a magnetized washer. Currents of 40mA and 60mA were applied, producing targets of 85 and 125μAm^2 respectively. The resulting dipole was oriented vertically (ie the plane of the loop was mounted horizontally). The washer had an unknown strength and dipole orientation.

The calibrated loop profiles were collected and gridded for presentation and analysis. Results from raw data produced contours consistent with synthetic models and are shown in Figure 6 and Figure 7. Amplitudes varied somewhat between the measured and synthetic responses, but may be the result of the very close proximity of the source to the sensor. The overall character of the signature shapes was excellent.
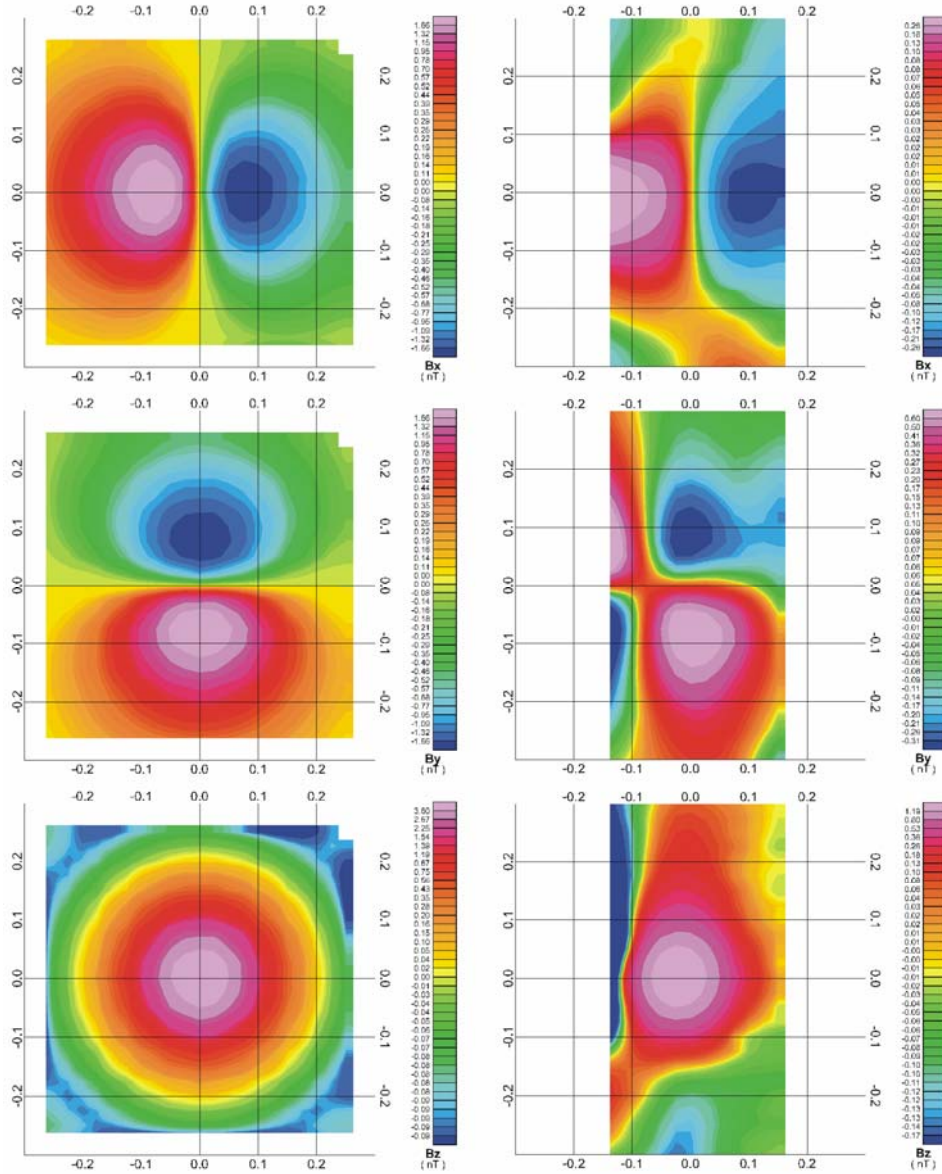
Figure 6: Comparison of synthetic (left) models of Bx, By, Bz (top to bottom) with measured SQUID (right) data from shielded test using an 85 μAm^2 locator loop as a vertical dipole source. Horizontal units in metres.
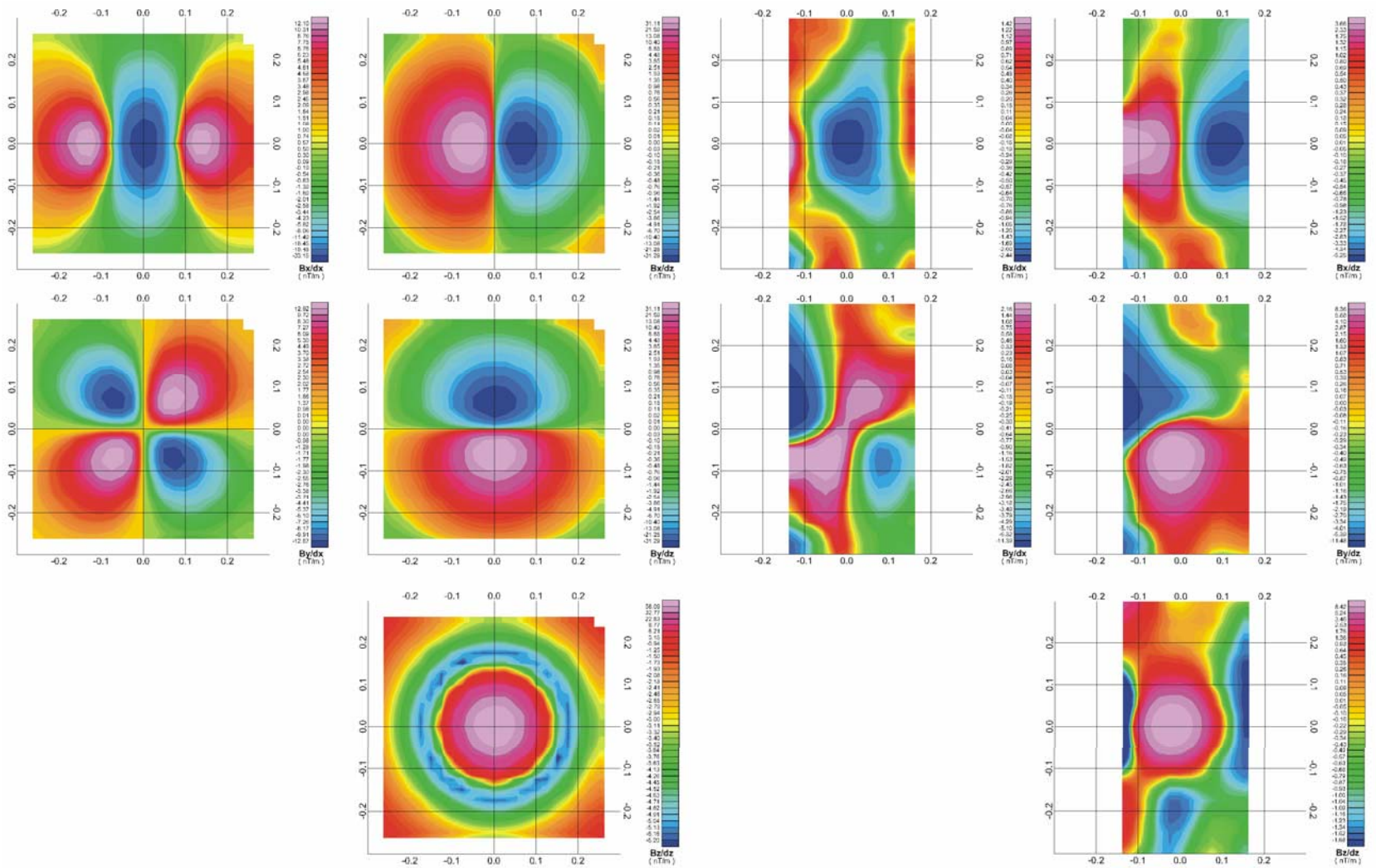
Figure 7: Comparison of synthetic (col 1&2) with measured SQUID (col 3&4) tensor gradients

Unshielded Operation

In August 2004, the SQUID sensor, dewar, electronics and recording system were operated in a relatively quiet unshielded environment. This was to prove whether or not the system can be operated outside of a shielded environment and verified a Go/NoGo decision point. It was determined that additional shields were required and these were built and tested in 2005 in a moderately noisy environment. A helicopter identical to the type proposed for the airborne platform was operated in close proximity to the sensor in order to verify that the sensor can be operated in an unshielded and high noise environment (see rotor noise). A final shield was constructed that included a mount for a fluxgate magnetometer that was physically attached to the SQUID core. This ensured consistent alignment between the two sensors between installations.

A layer of silver was originally added to the lining of the dewar when the slosh baffles were installed as a measure of RF-shielding. This proved to be inadequate in the field, as additional layers of aluminum foil were required to block sufficient background noise so that the electronics could lock onto a stable signal. Three layers of foil (approximately 1 mil each) were applied in order to damp background radiation to a sufficient level to achieve a signal lock.

Analysis of data using a 10kHz sample rate indicated that the SQUID did not reach a stable background level of white noise until above 100Hz. The maximum recording rate using the airborne console is 1200Hz. This limits the frequency bandwidth to 600Hz and below. This makes it difficult to establish an absolute noise level since the noise levels in the bandwidth of interest are frequency dependent. The difficulty in measuring noise levels in the frequency dependent response range is that a single number is inadequate. The power spectrum was useful in determining the peak frequencies of interest, but noise levels were better represented as an aggregate of the time series data.

Examination of either the time series or frequency spectrum data (recorded at 1200Hz) showed the clear dominance of 60Hz power line noise. Peak-peak 60Hz noise was measured as approximately 40nT in the total field (from the vector sum of the three components). Basic filters are sufficient to reduce the effects by two orders of magnitude. The on-board FIR filters used to desample the data from 1200Hz to 120Hz accomplish the same task when recording at the slower sample rate. Raw noise levels depend on the ambient power line signal at each site, and their interaction with the sensor. The distribution amongst the components and gradients depends on the orientation of the sensor with respect to the background field.

During these background tests, several data sets experienced sudden DC shifts. These were attributed to loss of signal lock in the FLL. This is most probably the result of signals exceeding the slew rate of the electronics (Koch, 1997). Since none of the signals within the observed bandwidth approached this limit, this was attributed to other signals beyond the range of the recording electronics (e.g. communications at GHz frequencies). These were blocked by constructing aluminum shields of various thicknesses.

Shielding calculations centered on the trade-off between RF-signal damping, and increased Johnson (thermal) noise and eddy currents. All three parameters increase with the thickness of the shielding. Attenuation of background and eddy current simulations were calculated based on a cylindrical model that allowed variable wall thickness and incident frequencies (Sarwinski, 1977). The relative shielding effectiveness for three aluminum shields and the foil used in these field tests are shown in Figure 8. Heavier shields produced additional attenuation, but with higher noise levels (Figure 9).
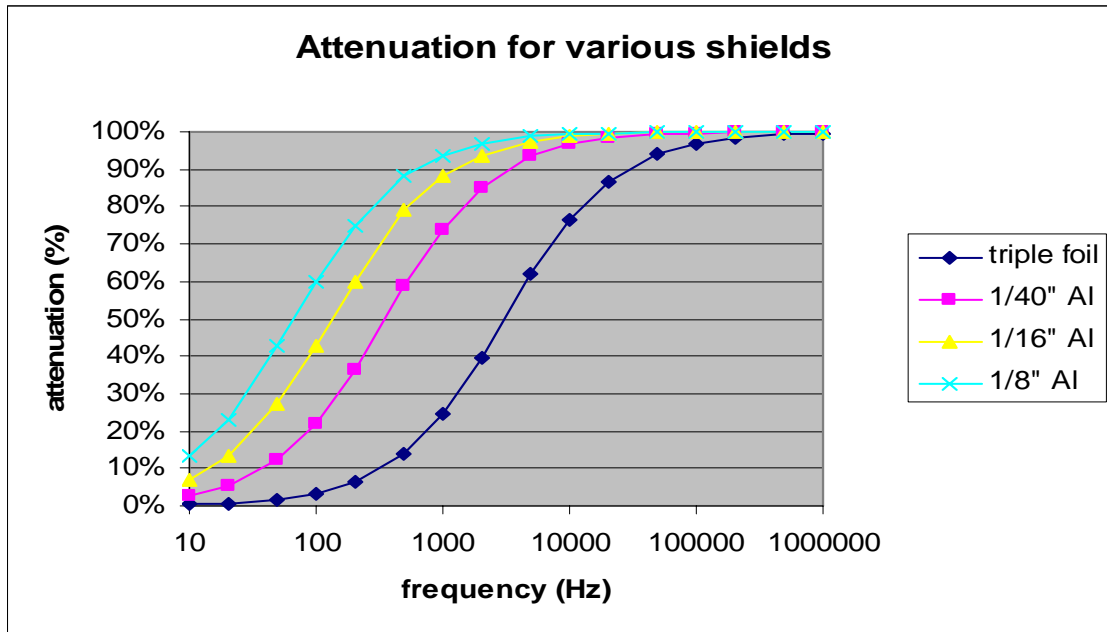
Figure 8: Amplitude attenuation vs frequency for four shielding options. Note that even the thinnest Aluminum shield increases 60Hz attenuation by an order of magnitude.
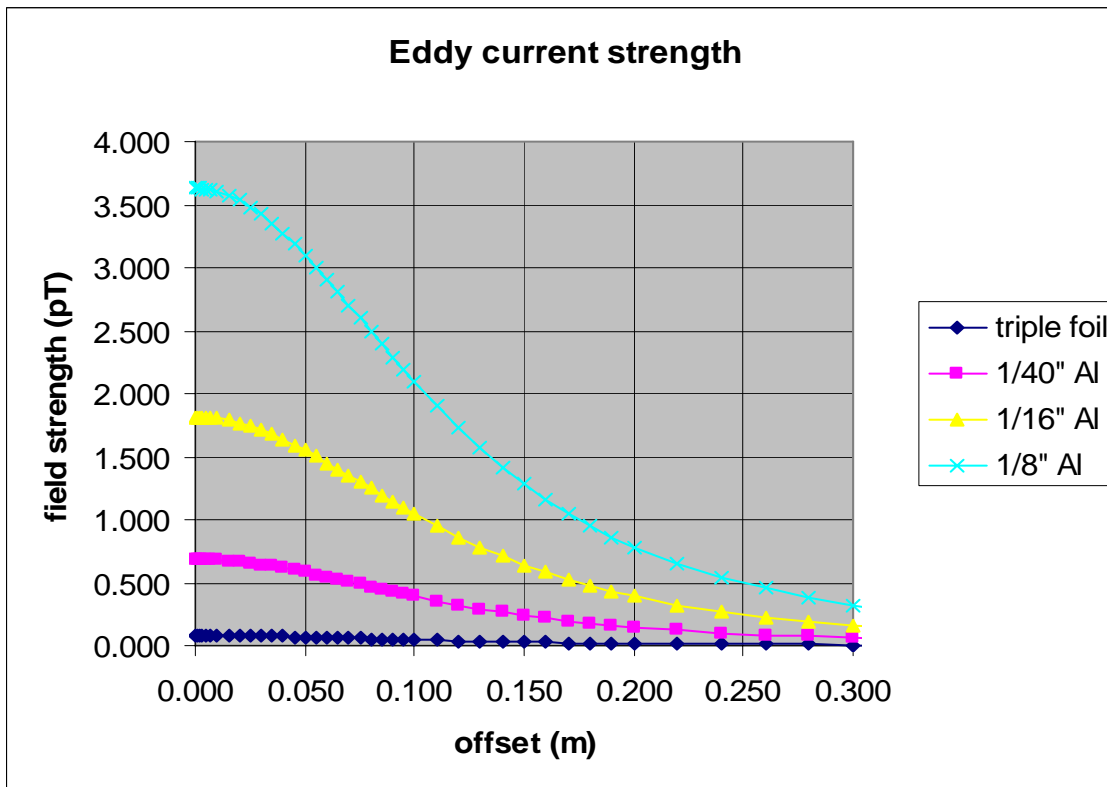
Figure 9: Eddy current field strength at various offsets from the geometric center of the shield. These plots assume a 60Hz incident field with a strength of 40nT. All SQUID sensors will be between 10-20cm from the center point.

Johnson noise is the result of thermal agitation of free electrons in a metallic body. This effect manifests itself as white noise with no spatial coherence. Shield thickness and distance from the shield are the key parameters (Varpula, 1984). Estimates showed noise ranging from 0.03-0.22 pT/rtHz for a cylinder based on the three aluminum shield thicknesses stated above, and an average 5cm offset from the nearest shield wall. These were well below the noise threshold established above, and so should did make a significant contribution to the overall system performance.

UXO Signatures

In order to determine the practical stand-off distance for the sensor, UXO target signatures were measured at the US Army Corps of Engineers Environmental Research & Development Center's UXO Test Stand in Vicksburg, MS (Figure 10). For these tests, the sensor was stationary on the test stand platform while the target was moved on a shuttle (Figure 11). The platform itself was limited to ±2m around the target. This was not quite large enough to capture the full signature of the response at these large offsets, but captured the peak/trough points on all but the By component at 3.5m, and the Bx and By components at 4.5m.

Targets included in the test were (in order of decreasing size) 155mm projectile, 120mm AT, 105mm HEAT, 105mm projectile, 2.75" rocket, 81mm mortar, 60mm mortar, 57mm projectile, 40mm mkII, M42, BLU26, 20mm projectile, and an M20 AT mine (Figure 12). Offset distances included nominal 4.5m, 3.5m, 2.5m, and 1.5m. Not all targets were used at all heights. The largest three were used only at 4.5m, as was the M20 AT mine. A single profile with the sensor in motion directly over a subset of targets was run at 0.5m vertical offset.

Maximum peak-peak deflections were calculated from the survey line where the target passed directly over the sensor. Signal-Noise ratios (SNR) were calculated for each target type and offset distance. Using a 10:1 SNR as a reasonable detection threshold, it was determined that a 60mm mortar could be detected at 4.5m, a 40mm projectile at 3.5, and a 20mm projectile at 2.5m.

Figure 10: ERDC UXO Test Stand prior to installation of canvas tent. Shuttle moves along top rails, while SQUID was stationed below the raised platform.

Figure 11: Photo of SQUID mounted on platform for 3.5m vertical offset tests. Inset shows small UXO target on mobile shuttle above the raised platform.

Figure 12: Photo of sample UXO targets used in experiment.

Using the 81mm mortar at a 1.5m vertical offset as a sample response and the noise levels calculated for this location, signal-noise levels were generated and shown in Table 2. Horizontal components have been ignored since they are orientation dependent. The signal levels for the Bx, dBx/dy and dBx/dz components should actually be near-zero along this profile, making the SNR calculation for these components irrelevant. Using the dBz/dz component as an example since it is the most rotationally invariant, signals and signal-noise ratios were calculated for several other UXO targets at various heights. The resulting signal-noise ratios are provided in Table 3.

Table 2: Response and signal-noise ratios for all tensor components for an 81mm mortar at a 1.5m vertical offset.

	signal	noise	SNR
Bz	10.74	0.042	255.7
dBz/dz	28.59	0.028	1020.4

Table 3: dBz/dz signal-noise ratios for various targets and heights. The red numbers correspond to target detection threshold objectives for the airborne project.

	4.5m	3.5m	2.5m	1.5m
105mm projectile	96.07	321.79		
2.75" rocket	31.07	83.93	169.29	1411.79
81mm mortar	15.71	58.93	119.64	1020.36
60mm mortar	9.64	26.07	57.14	453.21
57mm projectile	5.36	23.21	51.07	403.21
40mm mkII		11.43	26.07	183.93
M42			9.29	62.50
BLU26			9.64	44.29
20mm projectile			7.14	26.43

Orientation Issues

Several issues relating to orientation needed to be addressed. The first was how to relate the SQUID tensor data to an external frame of reference. This required a GPS/IMU capable of measuring platform orientation in the Earth's reference frame. This would give the instrument a positional accuracy of 2cm and an orientation accuracy of 0.01°. These were determined to be inadequate to create maps of de-rotated total field components, but it was sufficient for mapping tensor components and location of inverted target locations. A summary of the additional noise contribution to various parameters induced by an error in orientation is given in Table 4. This test also highlighted problems with the irregularity of the reset values, calibration coefficients and non-orthogonality of the SQUID elements.

Table 4: Noise due to unresolved orientation error.

Parameter	Additional noise due to orientation error
Profiles or maps of individual total field components	0.9-9 nT
Total field vector angles	0.01-0.015 °
Profiles or maps of de-rotated tensor gradients	0.0001 nT/m
De-rotated solution vectors which point to the target	2.6 mm.

The more important issue related to orientation was system performance on an oscillating platform. As vector sensors, the maximum signal change from maximum to minimum coupling will be a sine function with an amplitude of approximately 54,000nT/90° rotation (average 600nT/degree, maximum 940nT/degree). A helicopter in a hover is capable of rotating 90° in a few seconds. Assuming a uniform rotation speed, the result is a maximum rate of change of 42,300nT/s (940nT/degree x 45deg/sec). Accelerations (oscillations) produce even higher instantaneous rates of change. This greatly exceeds the capacity of the electronics to maintain a signal lock – the slew rate of the FLL. This can be mitigated by holding the SQUID in reset mode during turns at the end of each line. This reduces the orientation change to whatever the pilot can hold while surveying on line. The result is a lower amplitude change, but with oscillations over some relatively short time period. Previous measurements have shown flight parameters to be limited to ±5° in any direction (pitch, roll, yaw) with a dominant frequency below 1Hz. This limits the rate of change to an oscillating 10°/s (approximately 94,000nT/s) for worst-case coupling. This oscillation is expected to be on the edge of the instrument slew rate under more realistic coupling conditions. Measurements on a pivoting table were conducted to confirm the capability of the instrument.

The non-magnetic shake table facility at the Coastal Systems Station in Panama City Florida was used to test the SQUID response to orientation changes. This consisted of a pivoting table driven by three independent motors connected by belt drives (Figure 13). The speed and amplitude of the oscillation were set manually.

The platform was subjected to oscillations at various frequencies and amplitudes comparable to those expected in an airborne platform. Frequencies included 0.2Hz, 0.5Hz and 1.0Hz, and amplitudes included ±1°, 2°, 3°, 4° and 6°. At each combination of frequency and amplitude the pitch, roll and yaw were varied separately and then altogether. Finally the SQUID was rotated 45° on the platform and subjected to pitching motion only in order to equalize the horizontal component responses. The data were examined to determine if there was evidence that the maximum slew rate was being exceeded by these motions.
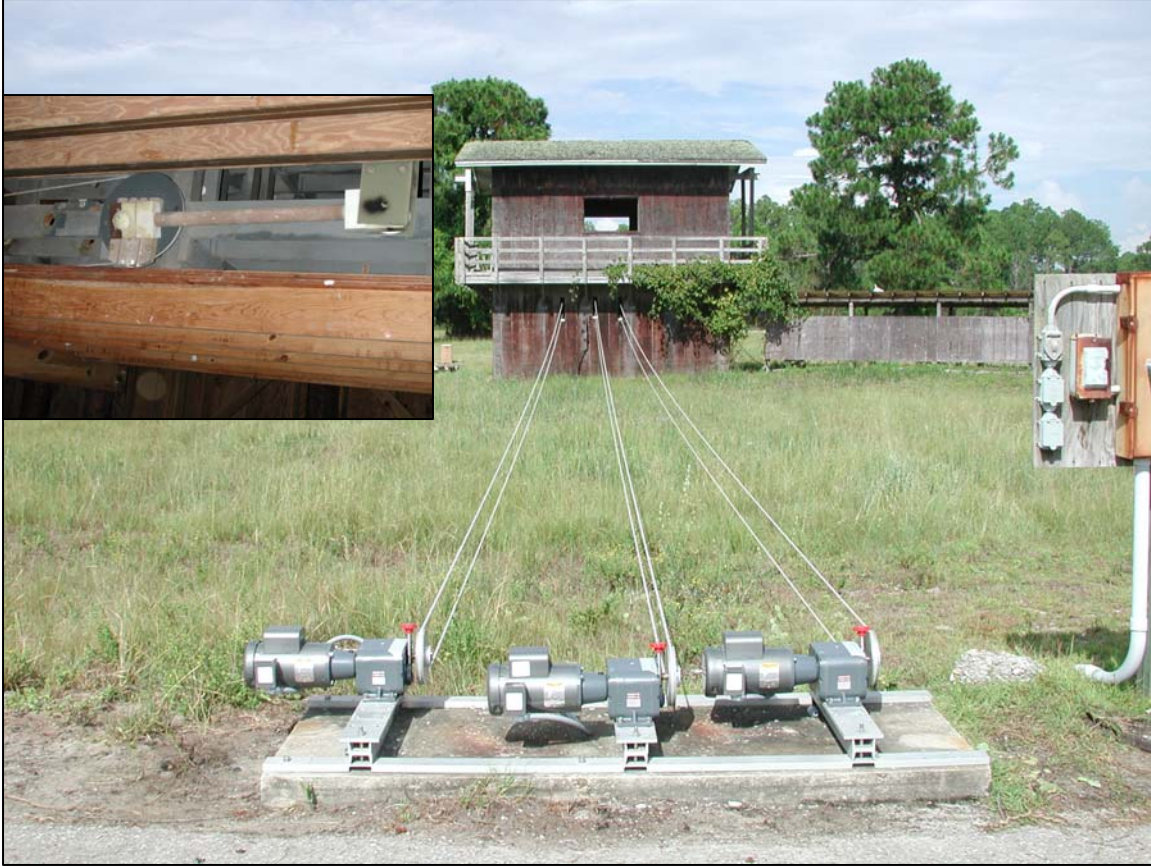
Figure 13: Photo of the CSS non-mag shake table facility. Motors control pitch, roll and yaw independently. Inset shows asymmetric piston controlling oscillation amplitude.

The data were analyzed by calculating the maximum instantaneous slew rate for each vector component. Calculations were made by taking the time derivative of the data between adjacent points in units of nT/s. The results for each component and combination of amplitude and frequency are shown in Table 5. In general, the Bx horizontal components (East) showed 1.5 times the rate of change of the By (North) component, and 3-4 times the rate of change of the Bz (vertical) component. This is a result of the relative coupling of each component direction with the ambient field. In spite of the high rate of change calculated from these data, no evidence of loss of lock was observed until the rates exceeded 42,000nT/s (Figure 14). This would imply that the slew rate is actually much higher than the 10,000nT/s previously predicted.

Table 5: Maximum rate of change (nT/s) by vector component for each combination of oscillation amplitude and frequency. Cells in red exhibited loss of lock.

		±1 deg	±2 deg	±3 deg	±4 deg	±6 deg
1.0 Hz	Bx	8550	18981	24282	34439	55404
	By	5472	12244	16758	24145	37620
	Bz	2462	5438	7558	11354	17784
0.5 Hz	Bx	4275	11867	13851	17852	42442
	By	2462	5917	8311	11423	41314
	Bz	1094	2668	3625	5027	18126
0.2 Hz	Bx	1881	4001	9747	6122	10499
	By	1163	2668	4617	4343	6327
	Bz	513	1197	1710	1813	2770
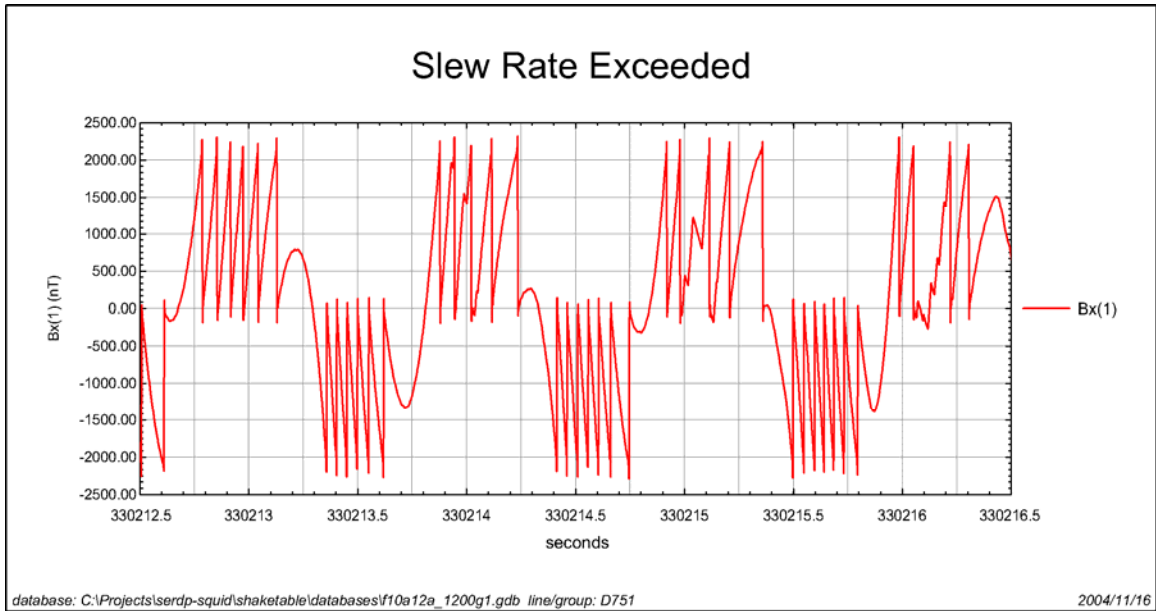
Figure 14: Raw profiles of the Bx vector data in nT. The breakdown of the smooth sinusoidal curve is the result of exceeding the instrument slew rate which causes the FLL to lose lock.

The frequency controls on the shake table were extremely difficult to set accurately, especially for low frequencies. The frequencies shown here are nominal. In particular, the timing of the roll control slipped in the "0.2Hz x ±3°" experiment and accelerated to closer to 0.4Hz. This accounts for the unusually high rate of change observed in this cell. Amplitude was also set manually and shows some deviation from the nominal values given here.

The oscillation tests on the shake table showed that the slew rate of the electronics was higher than originally anticipated (40,000 nT/s), but the maximum frequency and amplitude of the sensor oscillation was still approximately ±5° at 1Hz.

Non-Orthogonality and Calibration

The shake table tests highlighted problems with system gain calibration and the non-orthogonality of SQUID elements.

Tensor gradients are calculated as

dBx/dy = Bx(1) – Bx(2),
dBx/dz = Bx(1) – Bx(3),
dBy/dy = By(2) – By(3),
dBy/dz = By(1) – By(3), and
dBz/dz = Bz(1) – Bz(2).

By plotting these parameters from the oscillation data, it was found that the calibration factors were orientation dependent. If the sensor was rotated by 45°, the calibration coefficients changed significantly. It was also found that under certain oscillating circumstances, responses could be negatively correlated. Figure 15 shows how Bx(1) and Bx(3) are negatively correlated under a specific set of conditions.

It was determined that both of these effects were the result of non-orthogonality between sensors. This non-orthogonality has several implications. The principal problem is that each sensor is presented to the flux vector at a different angle. This causes a difference in amplitude that is quite separate from gain calibration caused by slight differences in sensor diameter. When the sensors are rotated this causes the observed peak amplitude to occur at a different time – a phenomenon which appears as a phase shift in the time series data. Under extreme conditions (Figure 15) this phase shift can be as great as 180°. This condition occurs when the flux vector bisects the angle between the sensors, causing one sensor to view the field as entering from "left hand" side, while the other views it as entering from the "right hand" side.
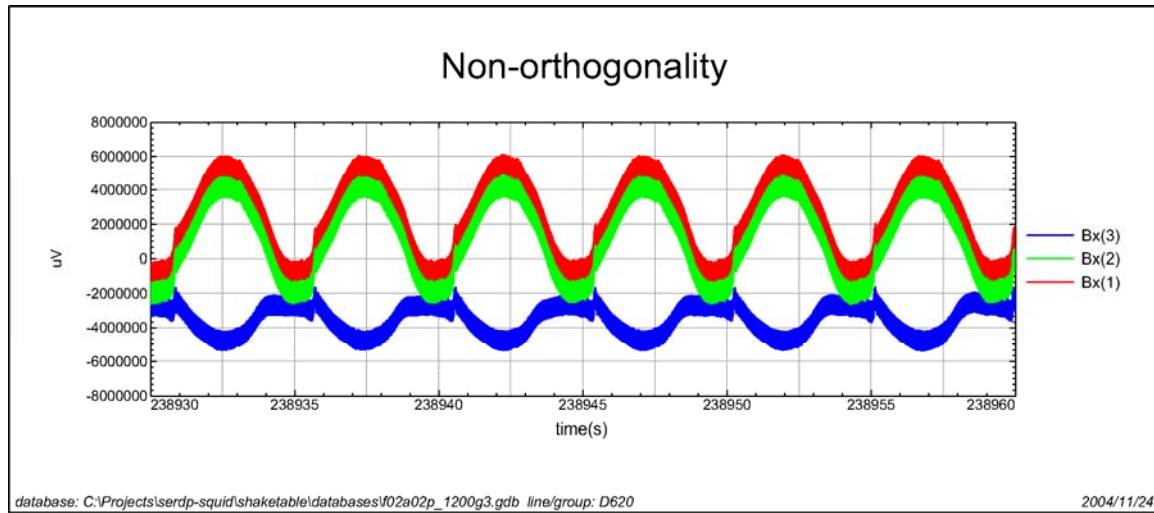
Figure 15: Profiles of the three Bx components during pitching motion. In this orientation the non-orthogonality of Bx(3) is clearly seen. The flux vector bisects the angle between Bx(3) and Bx(1,2) so that the changes in pitch appear to be 180° out of phase. Not shown at this vertical scale is the very high correlation in the 60Hz power line signal between all three sensors. (The thickness of the profile lines is the amplitude of the 60Hz signal.)

Another effect of the non-orthogonality is to introduce non-zero components to the tensor gradient data. In a uniform field, these parameters should be rotationally invariant. As can be seen in Figure 16 this is not the case. The gradient with the largest non-zero component is dBx/dz, which are derived from the Bx(3) with the greatest non-orthogonality.
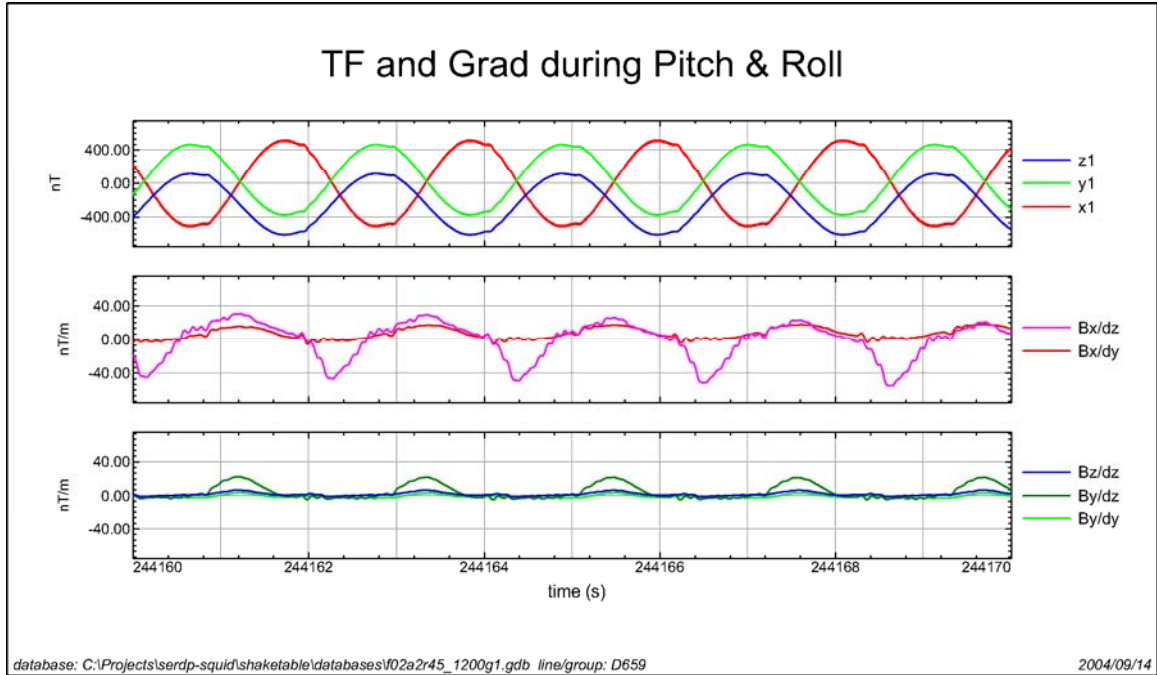
Figure 16: Profiles of total field components and tensor gradients during pitch and roll motion. Large amplitude total field responses are expected with changes in sensor orientation. Non-zero gradient components are largely the result of non-orthogonality between sensors.

Orthogonality measurements were based on the spin calibration equipment and algorithms developed by the USGS for their fluxgate magnetometer array. Upon deeper investigation, these proved to be inapplicable to the SQUID due to the nature of the system. An alternative was devised using the newly constructed USGS Helmholtz facility (Figure 17). This experiment was conducted in 2006, but a complete data set could not be collected. The digitally controlled coils exceeded the slew rate of the SQUID which lead to unstable readings. Additional problems with aging SQUID components also contributed to the experimental failure.

In 2007 a second test was run using the Billingsley Magnetics coil facility in Brookeville, Maryland, but this also proved unsuccessful. High noise from unshielded RS232 communications cables distorted too much of the data to render a complete data set.

Later in 2007, tests using a rotation turntable operated in an open field were conducted in order to compile a "limited" (non-3D) data set. This was a quieter environment, but revealed additional problems with the SQUID operation related to frequent system resets.
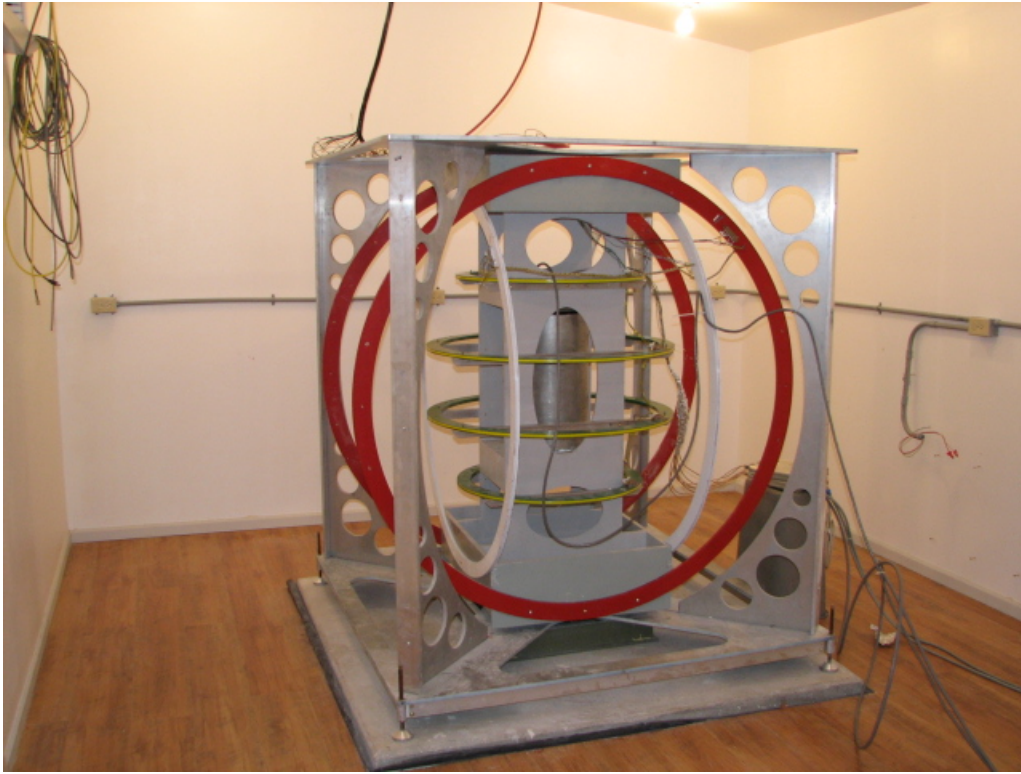
Figure 17: USGS Helmholtz coils with SQUID and fluxgate magnetometers installed.

A "limited" data set was collected using the USGS rotating platform. The problems associated with a digitally changing field were avoided, but a full tri-axial rotation of the field could not be achieved. Data were collected at a number of tilt angles to generate a data set that covered as wide an operating range as possible. A site at the local airfield was surveyed with total field magnetometers in order to pick an outdoor location with a minimal horizontal gradient. The SQUID was then mounted on the rotating platform at various tilt angles and data were collected throughout an entire rotation.

During these tests we found that successive resets caused by continuous rotation trapped flux within the SQUID elements. This trapped flux took several seconds to dissipate. The more often resets occurred, the more pronounced the flux trapping. This phenomenon manifests itself as a sudden dip in the data which slowly decayed back to its proper value. The resets are a normal system operation designed to maximize the dynamic range of the SQUID while retaining the highest possible resolution. When the SQUID response reaches the maximum voltage that the FLL can handle, the system resets to zero. These resets are tracked and the data are reconstructed in post-processing. We discovered that after approximately four or five resets in the same direction, this phenomenon became apparent and began to significantly affect the data. Resets in the opposite direction tended to counter act the opposing offsets, but reheating the element was the only certain way to eliminate trapped flux. Figure 18 shows data collected on a rotating platform. After each reset (vertical blue line) the SQUID response should continue its linear trend. By the end of the data sample the effect of the trapped flux is obvious even at this scale. The reason for this flux trapping is unknown.
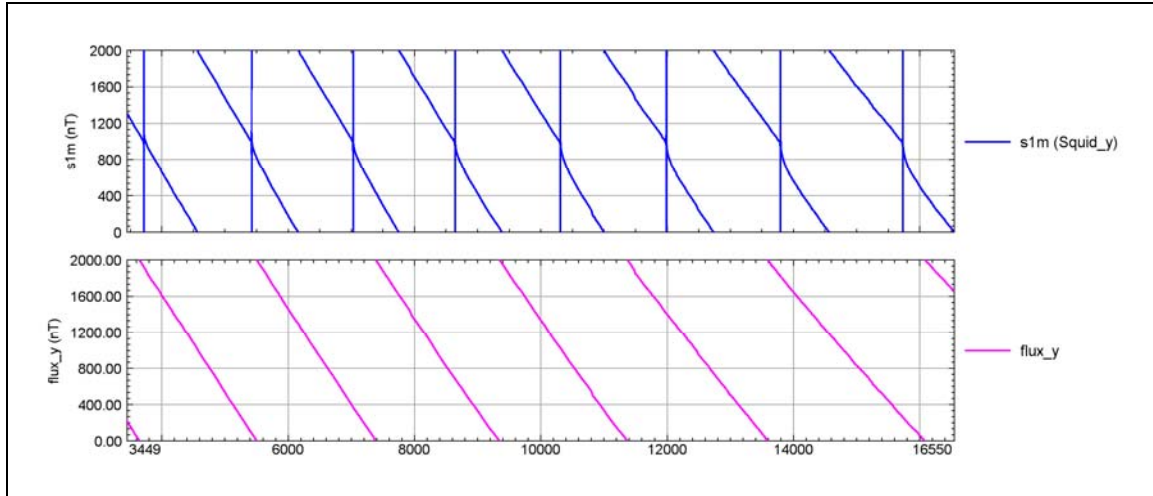
Figure 18: Plot of SQUID and fluxgate data from a rotating platform. The top window shows one of the SQUID y-components, bottom window shows the y-component of the fluxgate. The SQUID plot illustrates eight resets occurring within the SQUID data due to azimuth and magnetic field change. Flux trapping begins immediately on the second reset and becomes increasing more pronounced after each successive reset.

It was not possible to collect a complete rotation without resets and so no coefficients could be derived for the gain and orthogonality correction. Decreasing the gain to the point where the full +/-50,000nT dynamic range could be accommodated within a single reset would reduce the resolution but would be sufficient for a calibration set. This approach was considered but the manufacturer said that this was not possible.

Data Processing and Inversion

Development of data processing and inversion routine were an on-going part of the system development and testing. Processing routines are differentiated from inversion routines in that their scope is limited to converting sensor signals into final geophysical results. These were limited to previously known routines for positioning, gradient calculation, filters and calibration. As demonstrated above, these ran into insoluble problems with calibration coefficients and unexplained artifacts. Inversion routines take the geophysical data and calculate various target parameters. A systematic study of five approaches to inversion was conducted. Three were explored in detail.

- Dipole tracking (Wynn, 1975), an analytic solution of the tensor matrix on a point-by-point basis to locate a dipole source.
- Eigenvalues (Wilson, 1985), an eigenvalue solution of the matrix on a point-by-point basis to locate the target source.
- Tensor Euler (Zhang, 2000), a 3D tensor Euler solution of the gridded data to solve for target source location.
- Numeric Inversion (Heath, 2003), a multi-parametric inversion of the data to solve for target location.
- Rotational Invariants (Brown, 2004), mapping of rotationally invariant parameters to simplify visualization and point source location.

From the available literature, the invariants provided the best visual simplification of the data, whereas the Tensor Euler solution appeared to be the most accurate and stable of the target recognition approaches. The dipole tracking routine was also developed and tested.

Rotational Invariants

Tensor invariants are scalar values that can be determined from the tensor components. They are largely immune to orientation errors, making them excellent map products. As with total field and analytic signal maps, only variations in altitude between lines would create problems for these map products. They do not however, utilize the vector qualities of the SQUID system and therefore rely on densely sampled data. They may therefore be more profitably used to identify specific targets of interest (reducing the number of anomalies tagged for inversion), or to eliminate ghost solutions from inversion results. Algorithms for these parameters were developed and tested against synthetic data to verify their applicability.

Tensor invariants are described by several authors including Pedersen and Rasmussen (1990), Brown (2004) and Bracken (2004). Two tensor invariants and an associated dimensionless quantity are of interest:

$$\mathbf{I}_1 = \frac{\partial B_x}{\partial x} * \frac{\partial B_y}{\partial y} + \frac{\partial B_y}{\partial y} * \frac{\partial B_z}{\partial z} + \frac{\partial B_x}{\partial x} * \frac{\partial B_z}{\partial z} - [\frac{\partial B_x}{\partial y}]^2 - [\frac{\partial B_y}{\partial z}]^2 - [\frac{\partial B_x}{\partial z}]^2 \qquad (1)$$

$$\mathbf{I}_2 = \det(\,G) = \frac{\partial B_x}{\partial x} \{ \frac{\partial B_y}{\partial y} * \frac{\partial B_z}{\partial z} - [\frac{\partial B_y}{\partial z}]^2 \} + \frac{\partial B_x}{\partial y} \{ \frac{\partial B_y}{\partial z} * \frac{\partial B_x}{\partial z} - \frac{\partial B_x}{\partial y} * \frac{\partial B_z}{\partial z} \}$$

$$+ \frac{\partial B_x}{\partial z} \{ \frac{\partial B_x}{\partial y} * \frac{\partial B_y}{\partial z} - \frac{\partial B_x}{\partial z} * \frac{\partial B_y}{\partial y} \} \tag{2}$$

$\mathbf{I}_1$ and $\mathbf{I}_2$ can be combined to form a dimensionless quantity, $\mathbf{I}$, which is an indicator of two-dimensionality:

$$0 \leq \mathbf{I} \equiv - (\mathbf{I}_2/2)^2 / (\mathbf{I}_1/3)^3 \leq 1 \tag{3}$$

$\mathbf{I}$ is zero if the causative body is two-dimensional, and one for a monopole.
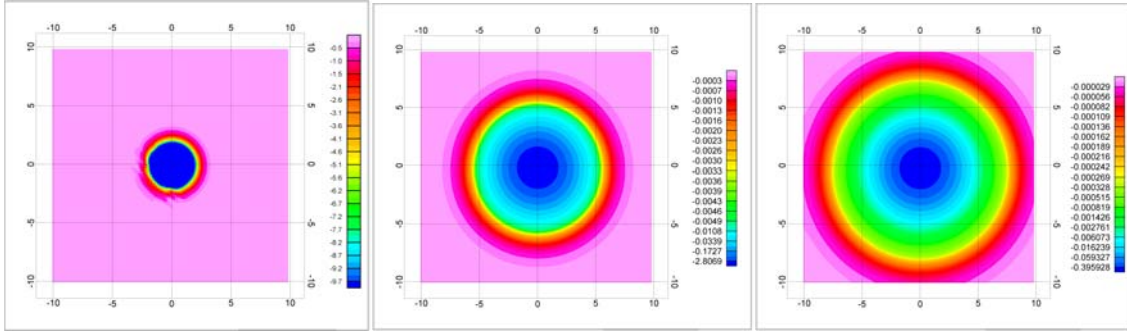
Figure 19: $\mathbf{I}_1$ **Invariant at 1, 2, 3m for the standard synthetic test dipole. Horizontal units in meters, data units in $(nT/m)^2$.**
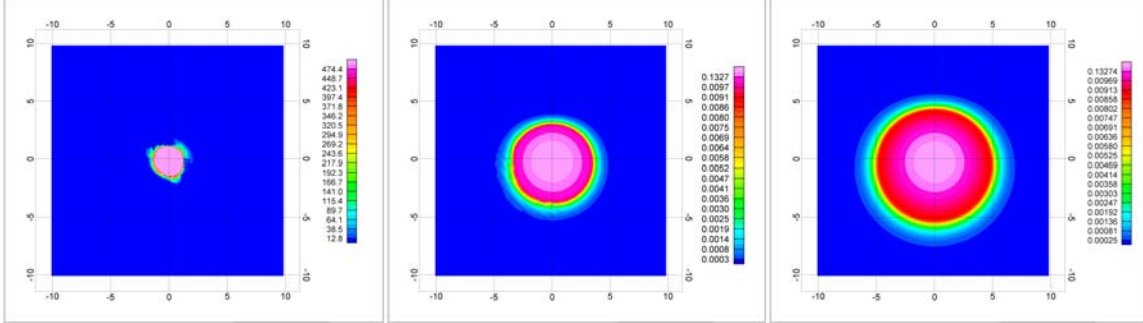
Figure 20: $\mathbf{I}_2$ **Invariant at 1, 2, 3m for the standard synthetic test dipole. Horizontal units in meters, data units in $(nT/m)^3$.**

A third tensor invariant, denoted as $\mathbf{I}_0$, is expressed as:

$$\mathbf{I}_0 = [\frac{\partial B_x}{\partial x}] + [\frac{\partial B_y}{\partial y}] + [\frac{\partial B_z}{\partial z}] = 0 \tag{4}$$

$\mathbf{I}_0$ is the trace of the G matrix, and is used to reduce the number of tensor components that must be measured in our instrument from nine to five. In our case, the $\frac{\partial B_y}{\partial y}$ component is calculated

from equation (4) so that fewer SQUID sensors are required in the instrument. If $\dfrac{\partial B_y}{\partial y}$ were measured in our instrument, Equation (4) could be used to assess noise in the system.

Dipole Tracking Alogrithm

These routines are based on detailed methods to invert magnetic gradient data published by Frahm (1972) and Wynn (1975) for the Naval Coastal Systems Laboratory (NCSL).

Dipole tracking is a point-by-point inversion routine often employed for real-time location of moving targets such as submarines. It inverts the tensor data to find a target location. This location is usually in the sensor frame of reference and must be de-rotated to an earth reference. The end result is a collection of points in space which represent dipole locations. Tight clusters of solutions represent reliable targets. This method determines the bearing to the dipole source and the ratio of the magnetic moment to the range to the fourth power. Once we have these two sets of information, we can use the total field data to find the range to the target.

The magnet field created by a dipole is given by:

$$\vec{H} = \frac{3(\vec{m} \cdot \vec{r})\vec{r}}{r^5} - \frac{\vec{m}}{r^3} \tag{5}$$

where $\vec{m}$ is the moment vector and $\vec{r}$ is the bearing vector, and r is the magnitude of $\vec{r}$.

This can be rewritten in the form:

$$H_j = \frac{3(m_i r_i + m_j r_j + m_k r_k)r_j}{r^5} - \frac{m_j}{r^3} \tag{6}$$

where i, j, and k represent the x, y, and z components of the respective vectors. The Frahm paper summarizes the computations required for deriving the bearing unit vector and the scaled magnetic dipole vector. The solutions are shown below.

The directional unit vector components, defined by $n_i = r_i / r$ are given by:

$$(n_1)_L = \pm\left(\frac{\alpha_{11}}{D_1}\bar{n}_1 + \frac{\alpha_{31}}{D_3}\bar{n}_3\right)$$

$$(n_2)_L = \pm\left(\frac{\alpha_{12}}{D_1}\bar{n}_1 + \frac{\alpha_{32}}{D_3}\bar{n}_3\right) \tag{7}$$

$$(n_3)_L = \pm\left(\frac{\alpha_{13}}{D_1}\bar{n}_1 + \frac{\alpha_{33}}{D_3}\bar{n}_3\right)$$

where the L represents laboratory coordinates and the bar over a symbol indicates values in rotated coordinates. The rotated values are given by:

$$\overline{n}_1 = \pm\sqrt{(a-b)/a}$$
$$\overline{n}_3 = \pm\sqrt{b/a}$$

(8)

where a and b are functions of the eigenvalues (∂H_i):

$$a = 2\partial H_1 + \partial H_2$$
$$b = \partial H_1 + 2\partial H_2$$

(9)

where the eigenvalues are designated $\partial H_1, \partial H_2,$ or ∂H_3 such that:

$$\partial H_1 \, \partial H_2 > 0$$
$$|\partial H_1| > |\partial H_2|$$

(10)

The scaled magnetic dipole moments as defined by:

$$M_i = 3\frac{m_i}{r^4}$$

(11)

are given by:

$$\overline{M}_1 = \pm\frac{1}{3}(5b-a)\sqrt{(a-b)/a}$$
$$\overline{M}_3 = \pm(5b-4a)\sqrt{b/a}$$

(12)

in the rotated coordinates and:

$$(M_1)_L = \pm\left(\frac{\alpha_{11}}{D_1}\overline{M}_1 + \frac{\alpha_{31}}{D_3}\overline{M}_3\right)$$
$$(M_2)_L = \pm\left(\frac{\alpha_{12}}{D_1}\overline{M}_1 + \frac{\alpha_{32}}{D_3}\overline{M}_3\right)$$
$$(M_3)_L = \pm\left(\frac{\alpha_{13}}{D_1}\overline{M}_1 + \frac{\alpha_{33}}{D_3}\overline{M}_3\right)$$

(13)

in the laboratory coordinates.

If we take equation 6 and solve for r, we should be able to find the range to the target.

$$H_j = \frac{3(m_i r_i + m_j r_j + m_k r_k)r_j}{r^5} - \frac{m_j}{r^3}$$

(14)

Substituting $n_i r = r_i$ as derived from the definition of r_j gives:

$$H_j = \frac{3(m_i n_i + m_j n_j + m_k n_k)n_j}{r^3} - \frac{m_j}{r^3} \qquad (15)$$

If we then substitute $m_i = (M_i r^4/3)$ from equation 8a we get

$$H_j = (M_i r n_i + M_J r n_j + M_K r n_k)n_j - (M_J r/3) \qquad (16)$$

or after solving for r

$$\frac{H_j}{(M_i n_i + M_J n_j + M_K n_k)n_j - (M_J/3)} = r \qquad (17)$$

This provides the range to target.

We now have a unit vector and a range to the target. Four solutions are generated, but three are ghost solutions which must be eliminated either by logic or through the convergence of multiple solutions.

Euler Tensor Inversion

The data generated by SQUID allows for the calculation of the full tensor matrix, as defined by equation 18 below.

$$T = \begin{bmatrix} T_{xx} & T_{xy} & T_{xz} \\ T_{yx} & T_{yy} & T_{yz} \\ T_{zx} & T_{zy} & T_{zz} \end{bmatrix} \qquad (18)$$

One analysis scheme that can be applied to magnetic tensor data is Euler Deconvoloution. The following equations form the foundation of this method.

$$(x - x_o)T_{xx} + (y - y_o)T_{xy} + (z - z_o)T_{xz} = -n(H_x - B_x)$$
$$(x - x_o)T_{yx} + (y - y_o)T_{yy} + (z - z_o)T_{yz} = -n(H_y - B_y) \qquad (19)$$
$$(x - x_o)T_{zx} + (y - y_o)T_{zy} + (z - z_o)T_{zz} = -n(H_z - B_z)$$

The variables x, y and z refer to the location of the SQUID, x_o, y_o and z_o refer to the location of the magnetic source, relative to the SQUID frame of reference. H_x, H_y and H_z are the magnetic field components generated by the source, while B_x, B_y and B_z are the components the background magnetic field. The structural index (n) depends on the shape of the target. If the source is a dipole, this value is 3.

This system of three equations has three unknowns, namely the difference between current x-position (x,y,z) and magnetic source location (x_o, y_o, z_o). The quantity $(H_i - B_i)$ can be

estimated by filtering background effects from the appropriate components of the SQUID. This set of equations can be written in matrix form of equation 20 as follows.

$$\begin{bmatrix} T_{xx} & T_{xy} & T_{xz} \\ T_{yx} & T_{yy} & T_{yz} \\ T_{zx} & T_{zy} & T_{zz} \end{bmatrix} \begin{bmatrix} \Delta x \\ \Delta y \\ \Delta z \end{bmatrix} = \begin{bmatrix} -n(H_x - B_x) \\ -n(H_y - B_y) \\ -n(H_z - B_z) \end{bmatrix} \tag{20}$$

This can be solved by finding the inverse of the tensor matrix and multiplying it to both sides. Once the location vector is calculated, it needs to be rotated, based on IMU data, to the local coordinate system.

The data flow is as follows:
1. Read in data, including SQUID location, field components, tensor data and IMU orientation data.
2. Find the inverse of the tensor matrix
   a. Find the determinate of the matrix
   b. Calculate the inverse by $\mathbf{A}^{-1} = adj(\mathbf{A})/\det(\mathbf{A})$
3. Find the offset vector by multiplying the inverse of the tensor matrix and the vector on the right side of equation 3.
4. Write output data to file, including current SQUID location and offset values to source location. Also include data needed in interpretation, including SQUID total field, IMU orientation data, and the determinant of the tensor matrix, which is tensor invariant I_2.
5. In Geosoft, convert the offset data from the SQUID frame of reference to the same frame of reference as the SQUID location. Subtract the offset from the SQUID location.
   a. Mask inversion results to either total field or I_2 values above desired threshold.

Figure 21 shows the ZZ component for a noise-free synthetic model with two sources, with both induced and remnant components. Although there is some scatter in the locations, there are two concentrations over the true location of the items. The addition of random noise produces a more random scatter of points but there is still a concentration of points in the correct place (Figure 22). If all points generated by data with a determinate of the tensor matrix less than 500 are masked, only concentration around the true locations remains (Figure 23). Increasing the noise increases the scatter, necessitating a larger determinate threshold.

If, however a DC offset is applied to the tensor data, the effect is different. A small offset (1 nT/m) causes the data to warp in a non-random way, as shown in Figure 24. There still is some concentration around the true locations, but there is also a structure to the scattered points. This suggests that an absolute value needs to be determined for the tensor data.

Euler deconvolution worked well on synthetic data, even with added random noise. However, it is extremely sensitive to non-random noise such as absolute offset of the tensor data. Accurate absolute values are difficult to achieve with real SQUID data which measures relative changes only. The results of deconvolution on real data sets show the same type of data scatter as the deconvolution of synthetic data with a DC offset. As a result, the Euler method may not be as robust as expected or required.

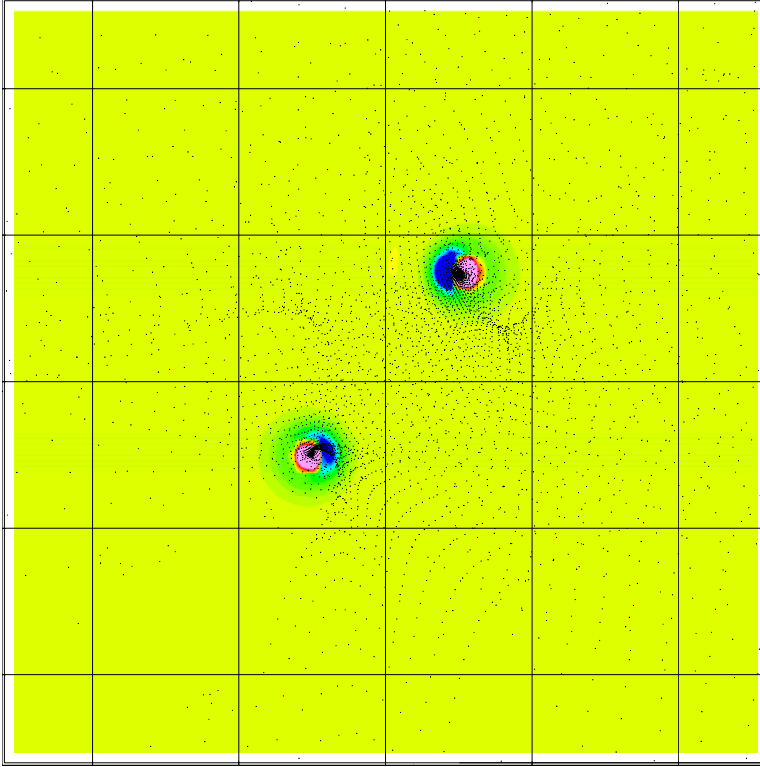**Figure 21: Inversion results for a synthetic model. The inverted locations are represented by the dots.**
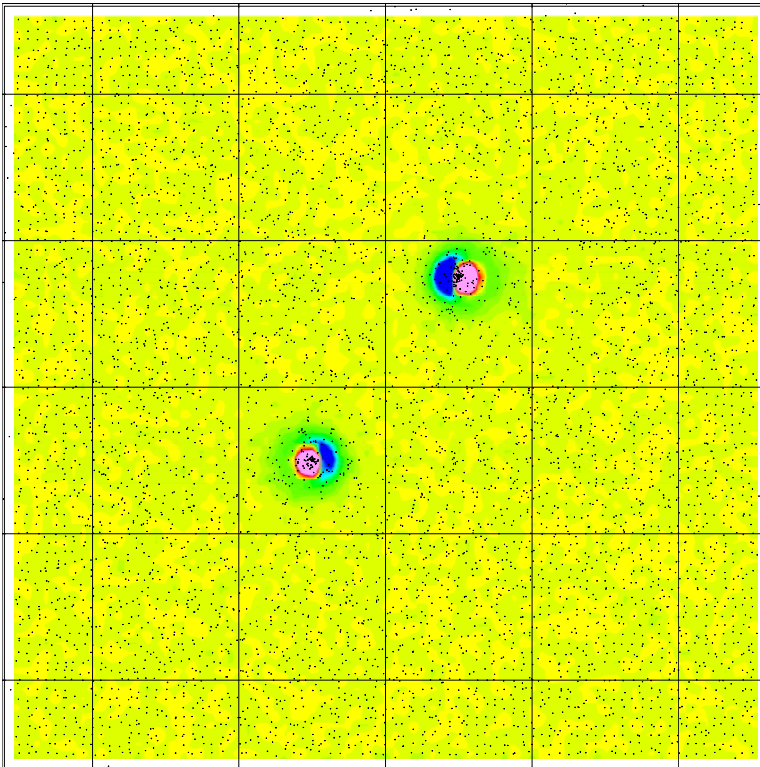

Figure 22: Inversion results from the noisy data shown in Figure 20.
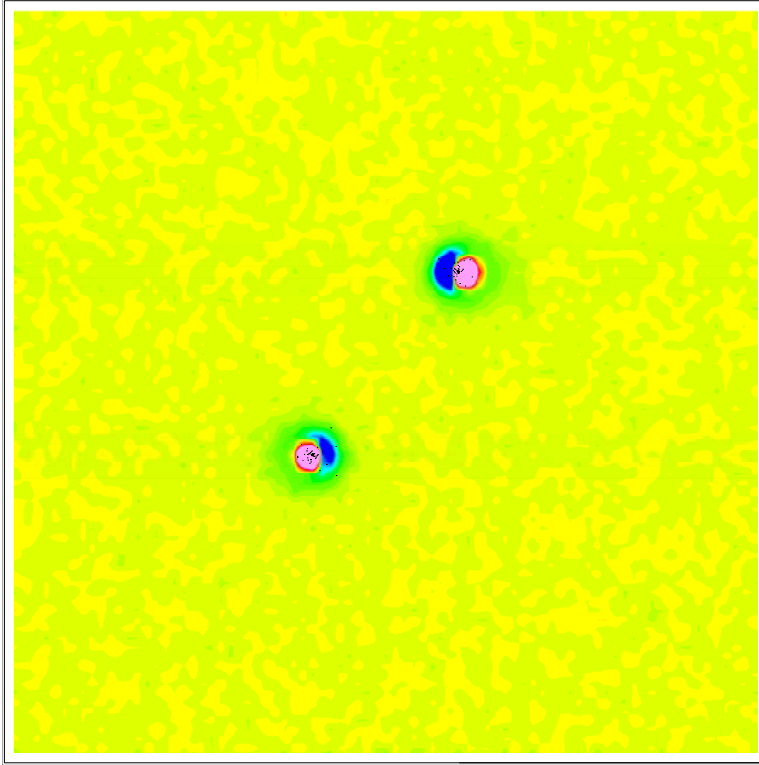
Figure 23: Same as Figure 21 but with all points generated from data with a determinant of less than 500 removed.
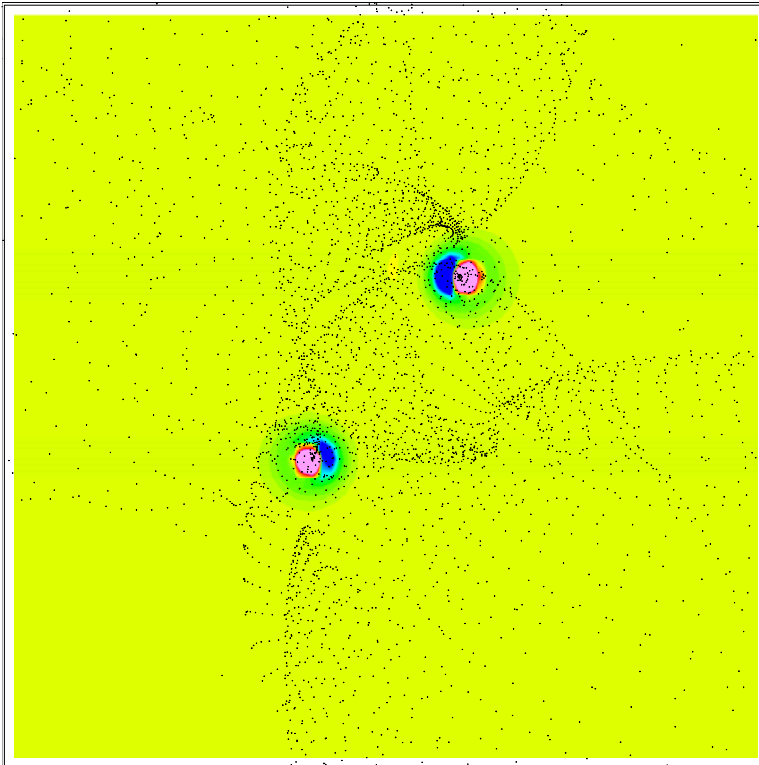

Figure 24: Inversion resulting from data with a 1 nT/m DC offset applied to all the tensor data.

Walk-over Survey at Test Grids

Ground tests over sample UXO targets were conducted additional funding provided by the Army Environmental Center. A unique field methodology was developed to avoid the known problems with the SQUID system. Ultimately, the combination of problems including frequent resets, sub-quantum data steps and generally unreliable system operation resulted in unsuccessful survey results.

Several walk-over surveys were executed to demonstrate the capabilities of the system on a moving platform including two complete test grids. A cart to transport the SQUID was obtained from Geometrics (Figure 25) and modified with a plywood shelves to hold the SQUID dewar, FLL electronics and GPS/IMU. The GPS antenna attaches to the top bars and can be positioned directly above the SQUID dewar. The IMU is placed near the operator at the back of the cart on a small plywood shelf. The IMU is stationed as far away from the SQUID dewar as possible in order to minimize interference.
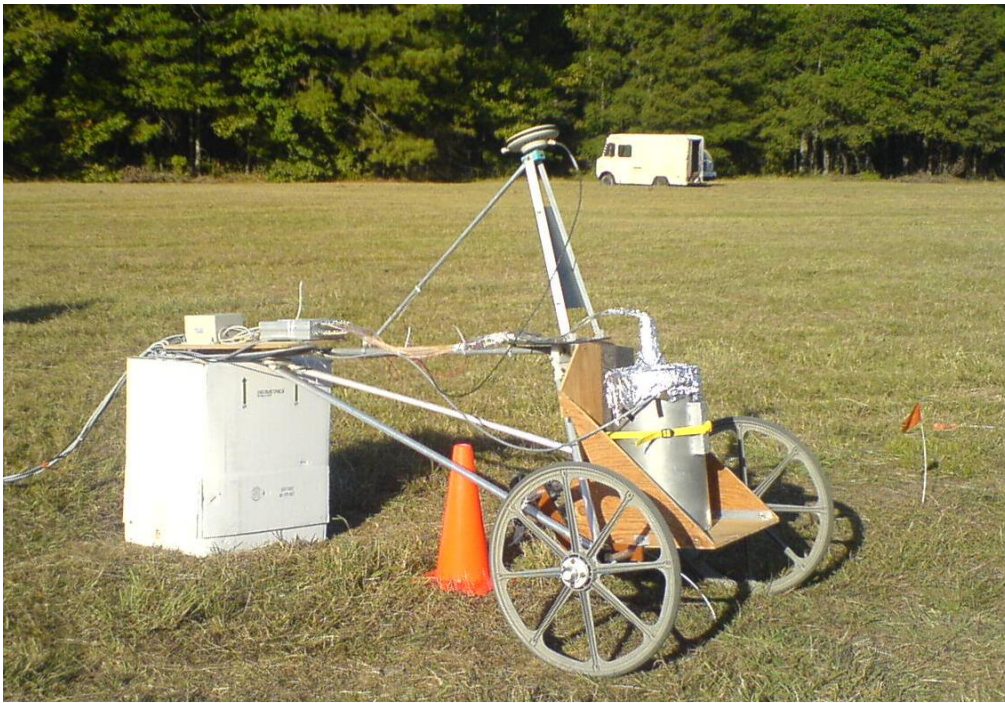
Figure 25: Photo of SQUID cart with dewar, FLL electronics and GPS/IMU.

Two surveys were conducted. The first was a test run over known surface items at the Oliver Springs Airfield. The second was an extended survey of the McKinley Range Geophysical Test Grid in Huntsville, AL.

Oliver Springs

The survey at Oliver Springs consisted of 35 survey lines spaced 1 meter apart (Figure 26). The lines ran southeast to northwest with the SQUID sensor approximately 3 meters ahead of the console. This orientation (console 3m SE of sensor) was maintained throughout the survey for consistency. Every effort was made to avoid unnecessary changes in SQUID orientation to minimize resets and avoid the flux trapping described above. At the end of each line the console and SQUID were reversed into place at the SE end of the next line. This minimized the

orientation changes of the SQUID sensor but maintained reasonable field productivity, since the alternative would be to heat and retune the instrument at each turn.

The survey grid at the Oliver Springs Airport was 34m x 50m. Seven metallic objects were placed on the grid including;

1) 2"long x 2.5"dia steel pipe (medium), vertical
2) One 20mm round
3) Clip of nine 20mm rounds
4) BLU 26mm
5) 2"long x 2"dia steel pipe (small), vertical
6) 3"long x 3"dia steel pipe (large), vertical
7) 2"long x 2"dia steel pipe (small), vertical
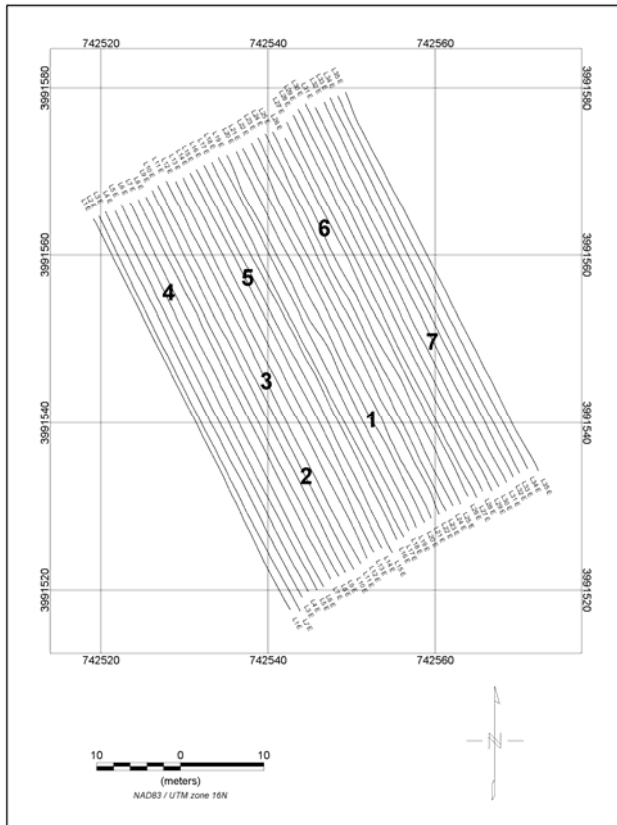
Figure 26: Line paths for the Oliver Springs survey. All lines were walked in a southeast to northwest direction. Numbers 1 through 7 represent the target locations.

Resets were present in the data as predicted, but were kept to a minimum by reducing the azimuth changes. Another problem observed in the data is the phenomenon of cycle slips. These occur when the FLL electronics temporarily lose lock on the signal and relock on the next quantum over – usually due to a rapid change in field strength. This produced a DC shift in the output data equivalent to one flux quantum. For our electronics, this is equivalent to approximately 1.14nT. Numerous slips were observed in the data, but these did not always correspond to increments of flux quanta. The source of these slips and their non-quantum nature has not been adequately explained by the manufacturer. During post processing most of the slips were removed. Slips which could not be removed appear as step features in the raw data but as dipole anomalies in the filtered data.

Figure 27 is the SQUID total field data over the site, while Figure 28 is the fluxgate total field. The SQUID total field shows four of the seven targets, while the fluxgate total field identified all seven. Four of the UXO targets produce anomalies large enough to be seen over the noise threshold in the SQUID total field. The remaining anomalies have a smaller signal and cannot be seen over the noise. When the SQUID total field data were gridded with a lower threshold, three more of the UXO targets appeared on the grid, however, noise levels increased dramatically. The noise produced from the cart's movement creates a variation of approximately 70nT in the raw data. Most of this noise is removed using the low pass filter. The additional anomalies seen by the SQUID are spurious features rather than anomalies missed by the fluxgate since they did not appear on the pre-seed survey.
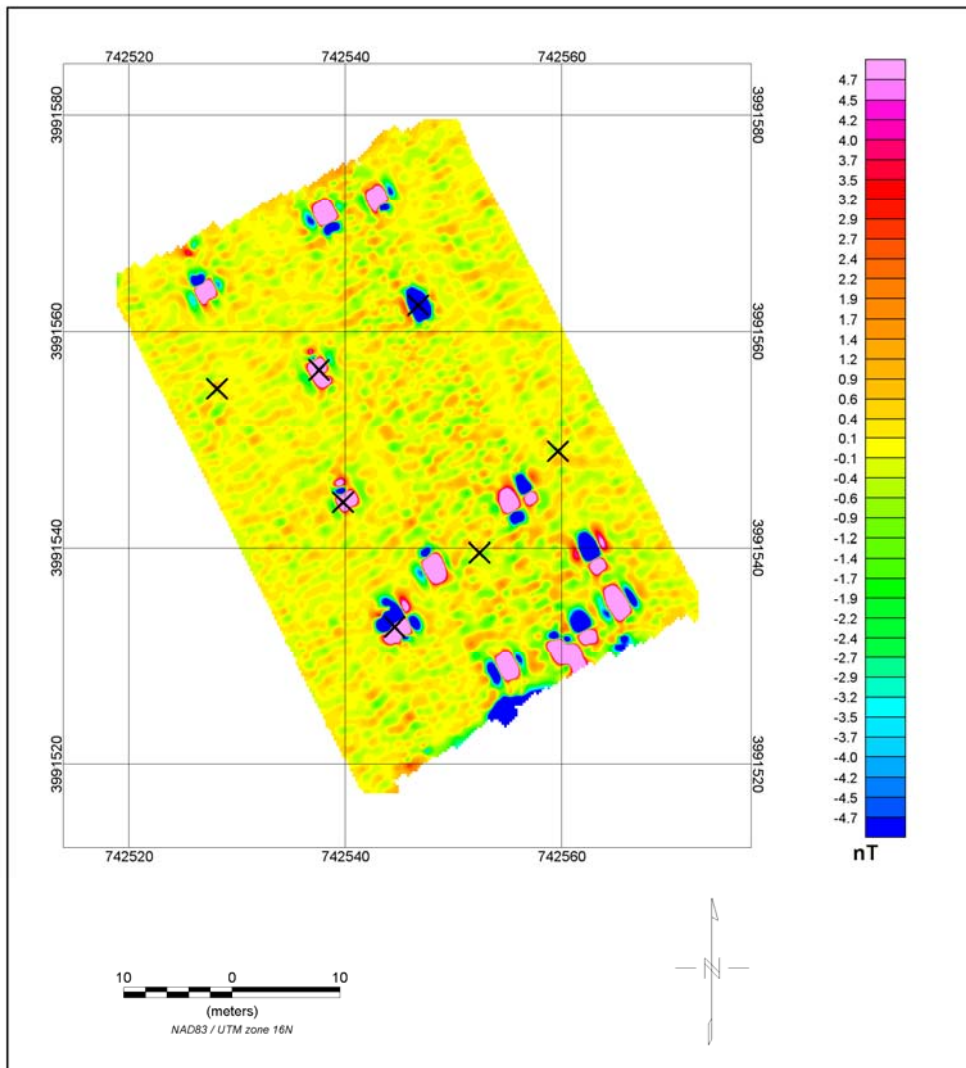
Figure 27: Plot of the SQUID total field, calculated from the x, y, and z-components. Offsets and cycle slips have been removed from the data. X's mark the target locations for the seven different UXO objects. Four of the objects were successfully identified using the SQUID system.
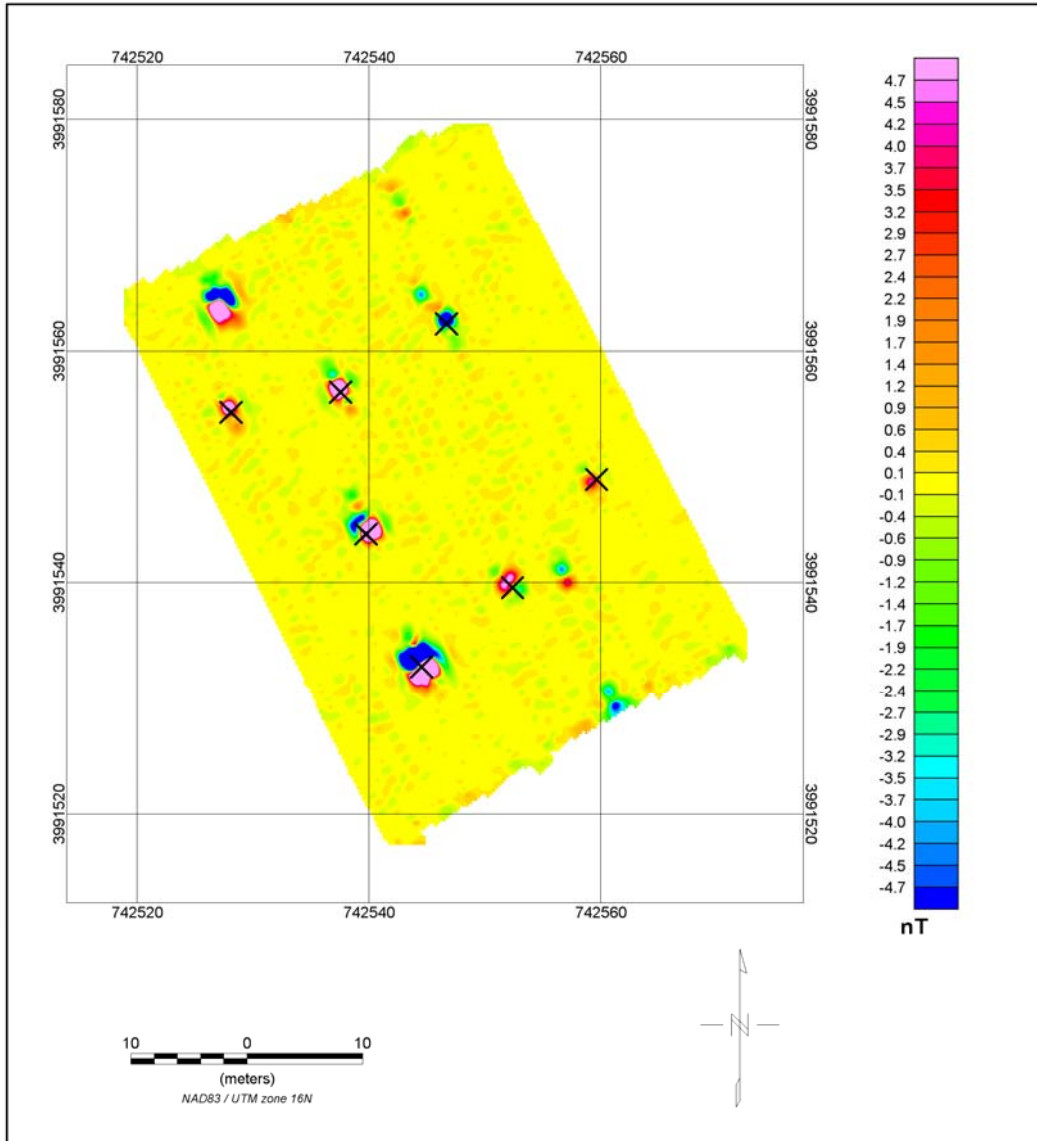
Figure 28: Plot of the fluxgate total field, calculated from the fluxgate's x, y, and z-components. The X's mark the target locations. The fluxgate successfully identified all of the seven target items.

Figure 29 shows inversion results from McKinley overlaid on a grid of the zz tensor. The same type of scatter is observed here as in Figure 24 where a small offset was added to all tensor data. In the real data the problem is more severe, making it impossible to locate targets using the inversion results.

The best that can be done with real data is to set the average to zero, which was attempted but without success. A possible solution to this problem is to use the fluxgate to set the baseline for the tensor data. However, in order for this to work the relative position of the fluxgate to the SQUID elements would have to be known to high degree of precision.
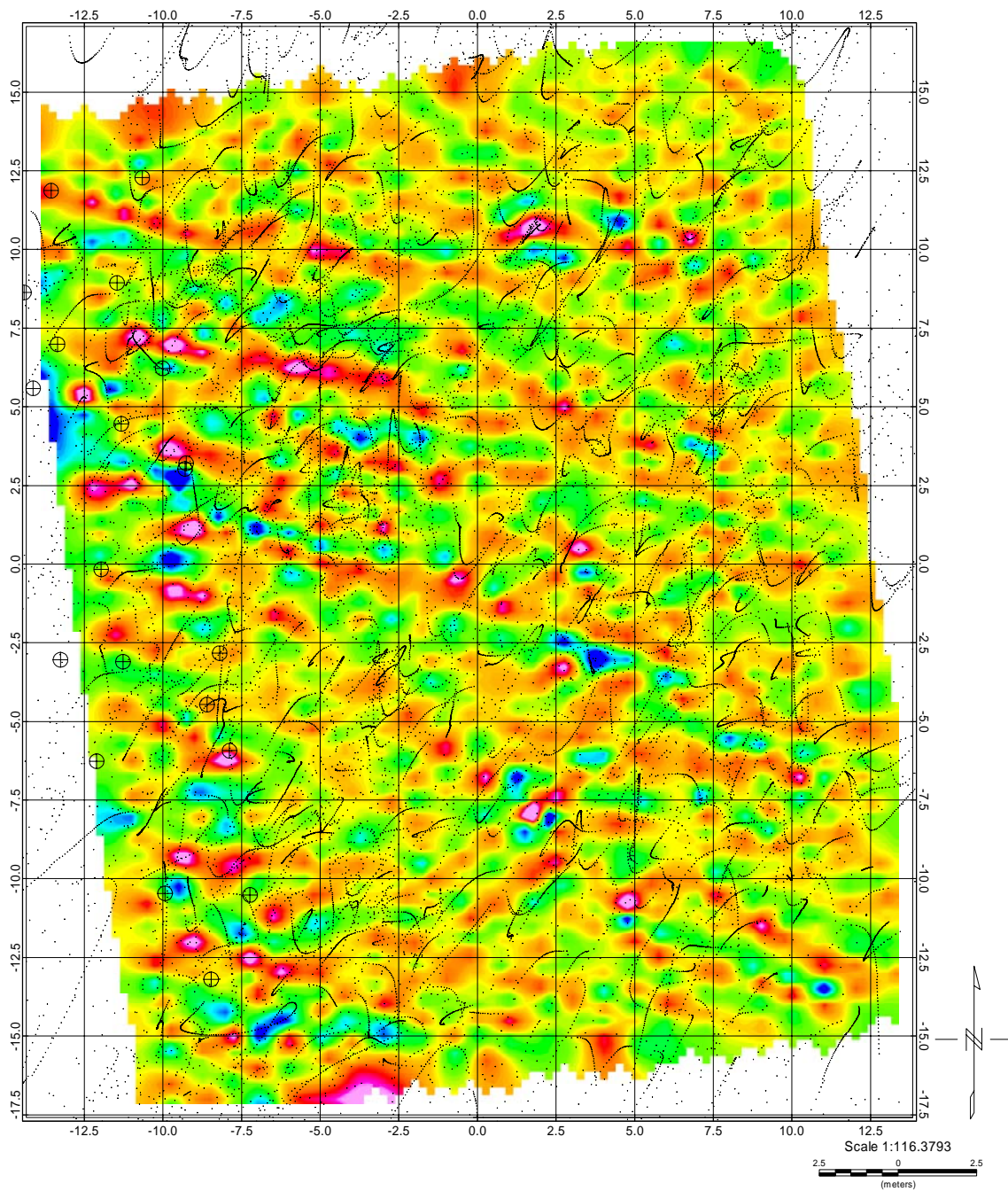
Figure 29: Field data (zz tensor shown) collected at the McKinley test site with inversion results.
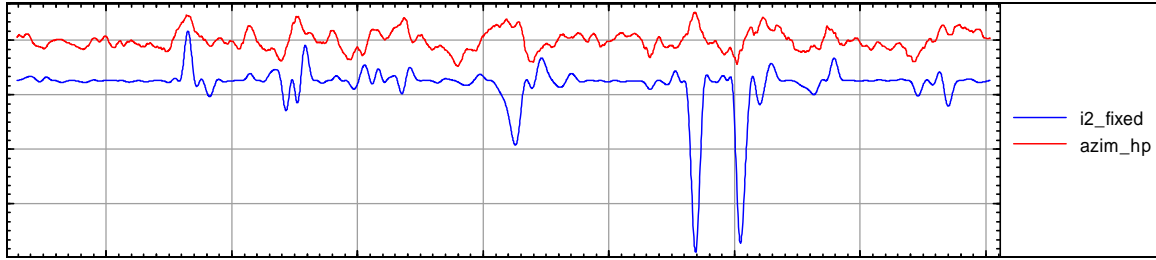
Figure 30: Invariant I_2 (blue) and azimuth (red). Note the correlation between the two, which should not exist if I_2 is truly invariant.
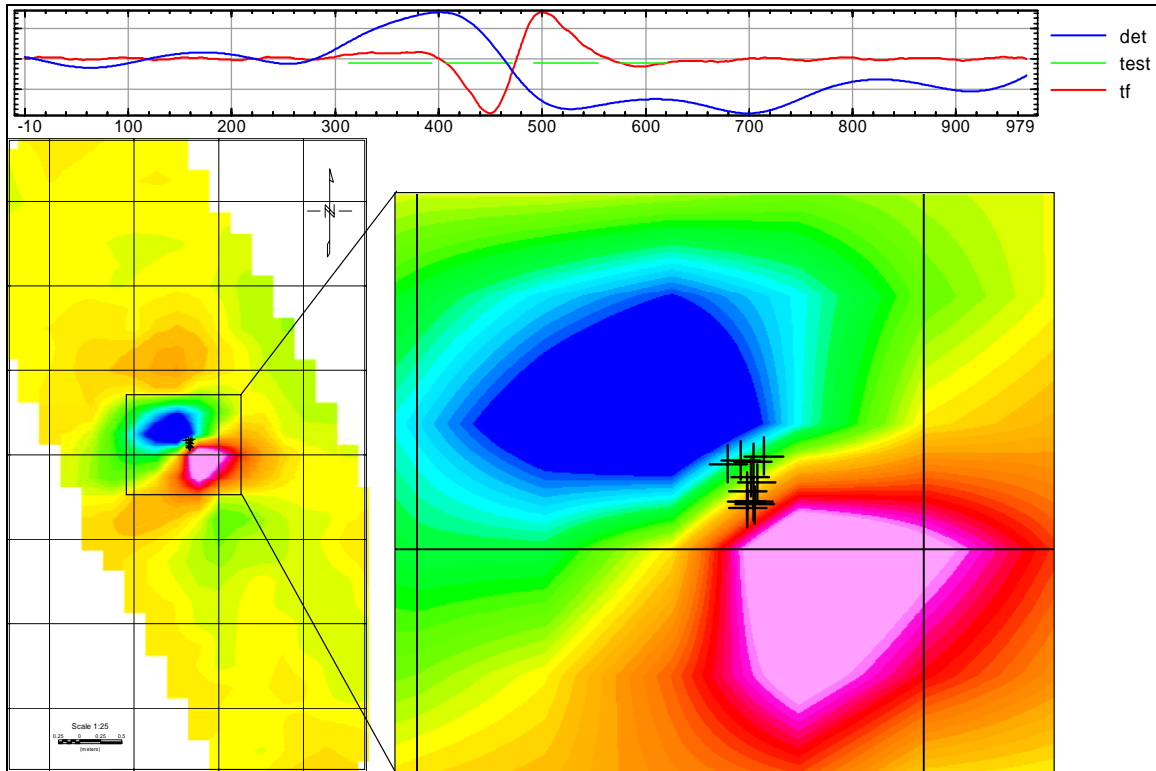
Figure 31: Extract of McKinley test grid data. Top: profiles showing the determinant, total field, and mask applied to map (bottom) of total filed data with inverted locations. Inversion results masked to the total field values of at least 170 nT.

Another reason that the inversion might be failing is that the SQUID elements are not orthogonal. This would also explain why the invariant I_2 is not invariant, as demonstrated by Figure 30. This shows I_2 and the azimuth from the IMU. If I_2 is invariant, then it should not show any correlation to the direction of the SQUID. However, the figure clearly shows a strong correlation between the two.

The best result obtained with real data is an inversion over one line of data from Oliver Springs (Figure 31). This line was selected because the anomaly has a relatively large signal-noise ratio. The tensor data was low-passed before inversion.

McKinley Range

After testing at Oliver Springs Airport, the system was deployed at the McKinley Range, Huntsville AL in October 2007 for testing at the HNC UXO test site. This test site is broken into five 100′x100′ grids, one of which is seeded with inert OE items from 20 mm rounds to 2,000 lb bombs with depths from a few inches to nearly 10 ft.

This site was surveyed from north to south, with the SQUID cart always to the south of the console cart (Figure 32). As before, at the end of each line the console and SQUID were reversed into place at the north end of the next line. This minimized the orientation changes of the SQUID sensor and avoided previously observed problems with rotation changes. The survey consisted of 31 survey lines spaced one meter apart. After every six lines the SQUID components were reheated. This was done in order to clear out any trapped flux caused by the resets.

Figure 32: Photo of the SQUID system setup at McKinley Test Range, Huntsville, Alabama. The SQUID cart was always positioned south of the console and was pushed down the survey line and pulled in a zig-zag direction back to the next line. Spacing between the console and the SQUID dewar was approximately 3 meters.

After line 24, channel 4 began to drift uncontrollably and could not be stopped even after successive re-heating and tuning. The instability in this channel, presumably trapped flux, was strong enough that the effect distorted the field in neighboring SQUID elements and increased the low frequency noise throughout the system. The data from line 25 through line 31 was removed from the final calculations and mapping due to the large drift by channel 4.

Resets and cycle slips occurred throughout the McKinley Test Range data on all channels and were removed with the same routine as was used on the Oliver Springs survey data. The SQUID total field data was calculated from the SQUID components (Figure 33) and compared to the fluxgate total field data (Figure 34) as before. Targets are defined in Table 6 and are marked on both total field maps.
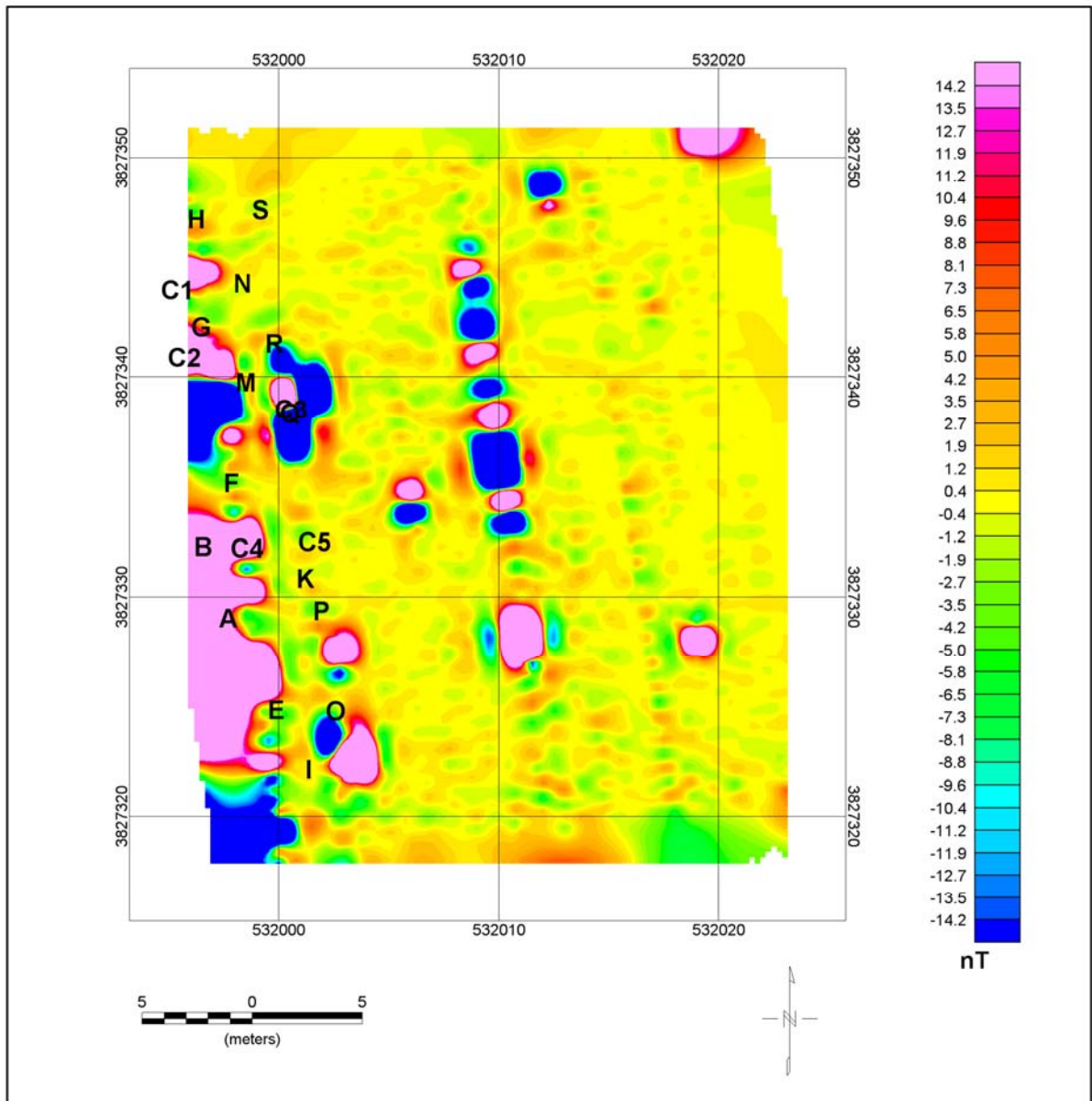
Figure 33: Plot of the SQUID total field data at McKinley Range. Target locations are lettered on the grid. The SQUID total field identified nine of the twenty seeded UXO items.
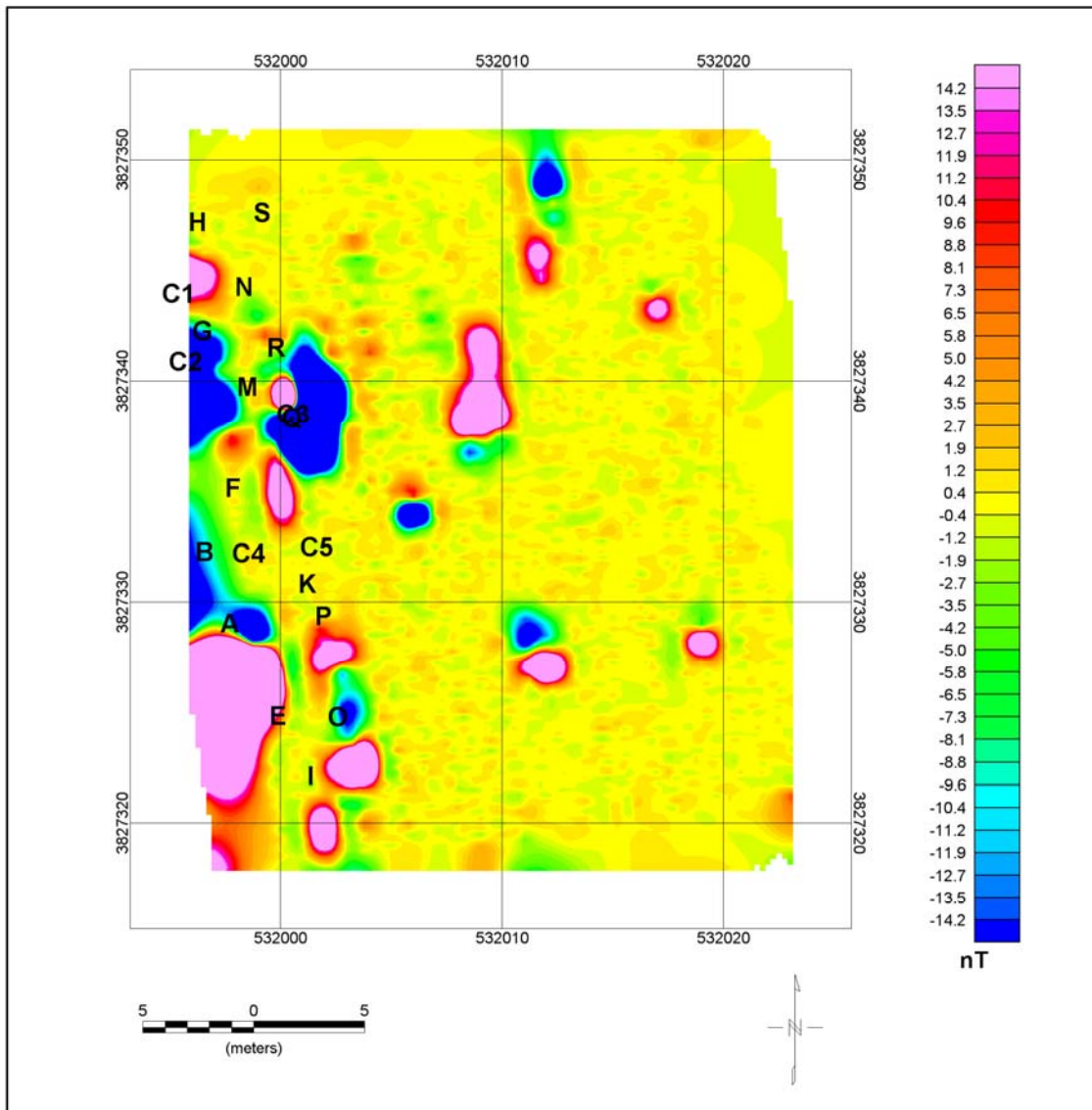
Figure 34: Plot of fluxgate total field data at McKinley range. Target locations are plotted as letters on the grid. The fluxgate identified eleven of the twenty seeded UXO items.

The total field data from the McKinley Test range survey was noisy due to the cart's motion. We calculated the invariants in an attempt to minimize this noise and maximize the target anomalies. The profiles of the three invariants are plotted in Figure 35, as well as the SQUID and fluxgate total field for comparison. Each of the three invariants appear similar, however, the "bouncing" of the SQUID cart still exists in the data.

Table 6: Twenty seeded UXO objects in the McKinley Test Range.

ID	Item Description	Detected by Fluxgate	Detected by SQUID system
I	2-105mmProjectiles	no	no
E	150mmProjectile	yes	maybe
O	105mmProjectile	yes	yes
P	8inchPieceof#6Rebar	no	no
B	30mmPracticeBomb	maybe	yes
K	2-155mmProjectiles	no	no
A	8inchProjectile	yes	yes
F	2-M43Submunitions1.07	no	no
C5	Handful of Roofing Nails	no	no
C4	Handful of Roofing Nails	no	yes
Q	155mmProjectile	yes	yes
C3	Handful of Roofing Nails	yes	yes
M	3-155mmProjectiles	no	no
C2	Handful of Roofing Nails	yes	yes
C1	HandfulofRoofingNails0.15	yes	yes
G	155mmProjectile	maybe	maybe
R	2.75inchRocketwithFins2.03	no	maybe
N	4.2inchMortar	no	no
S	M39Submunition	no	no
H	75mmProjectileHEplusCase0.91	no	no

Figure 35: Profile plots over calibration lane. Top: the invariant, I_1, Second: I_2, Third: SQUID total field, Bottom: fluxgate total field.
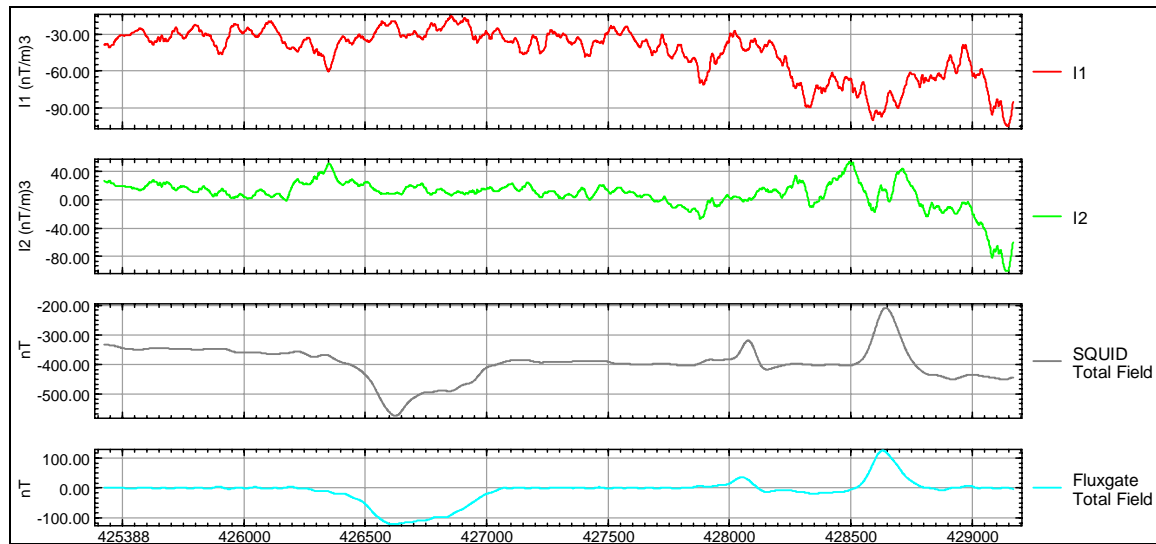
Conclusions

SQUID sensors are highly sensitive and complex instruments. Numerous successes and valuable lessons have been learned in the course of this project and they should not be overshadowed by the disappointment of the field deployments. The instrument used in this project functioned extremely well in a stationary mode. Noise levels in both shielded and unshielded environments were low and response linearity was good. Sensor orthogonality was not as good, but even the worst combination of elements appeared to be within 0.5°. Sample UXO targets were detected at considerable distances with good signal-noise ratios. Vibration tests of the helicopter booms and rotor noise studies were all within reasonable limits. Data processing and inversion algorithms were researched and tested with synthetic data and were shown to be highly successful.

The transition to a moving platform, however, was ultimately unsuccessful. The mechanisms designed to allow it to function within a larger range of field values were sound and have been successfully deployed in other systems. With this system, they introduced unusual artifacts into the data which negated the possibility of completing basic calibration procedures. Even when avoiding these artifacts, continuing problems with random data shifts introduced so much noise that results were generally poorer than the supplementary fluxgate magnetometer. The lack of an absolute reference made quantitative analysis impossible for all but the strongest anomalies. The final result is that the operational noise level is so high that it outweighs the additional benefit of interpreting full tensor data for UXO detection.

Overall system problems can be divided into two overlapping categories: operations and calibration. Operational problems included flux trapping and cycle slips. Calibration issues included inconsistent reset values and an inability to collect an adequate data set for gain and orthogonality coefficients. Taken together, these problems led to an inability to produce any map products which demonstrate the inherent benefits of SQUID sensitivity and tensor data collection.

Small instances of flux trapping were observed at each successive reset with cumulative effects. No explanation was ever found for this effect, but the only solution was to reheat and tune the sensor (essentially reboot). Large amounts of trapped flux occurred when the system was jostled. This resulted in output data that were completely unrelated to changes in ambient field strength. Furthermore, the effect was strong enough that it was observed by adjacent SQUID elements and corrupted that data also (e.g 2007 McKinley Range test).

Cycle slips appeared to some extent in virtually every data set. In theory, these should have been increments of flux quanta, making them readily identified and removed. In practice, steps of all sizes were observed. Some steps were so small that they could not be positively identified as cycle slips, but they brought the quality of the entire data set into question. After standard data processing procedures, unresolved cycle slips appear as simple dipoles in one or possibly two of the gradient tensor components thereby increasing the false positive rate.

Like the cycle slips, the reset values did not conform to expected SQUID theory and no sufficient explanation was ever found. These should have been consistent within one flux quantum, but again, a wide range of values was observed. Also like the cycle slips, the false DC offset had a cumulative effect on the accuracy of absolute readings and appeared as a false dipole after standard data processing.

In the case of the gain and orthogonality calibration, the operational issues prevented collection of the complete data set required to derive the necessary coefficients despite three separate attempts conducted with the assistance of the USGS group, which had successfully developed and applied similar procedures for fluxgate devices.

In addition to these regularly repeating problems, the system continually proved to be too delicate for field deployment. On nearly every occasion in which the SQUID was taken to the field, or when laboratory measurements were being made, some component of the system failed. In some cases, the problem could be rectified by reheating, retuning, or through unexplained recovery. In other situations, it took a few months to repair, and had to be returned to the manufacturer. Although some of these repairs resulted in substantial performance improvement, we must conclude that the system as it is currently configured (high temperature, vector components) is not sufficiently robust for routine field operations.

This should not be considered as a blanket statement covering all SQUID technology however. This system was a high temperature component system originally designed for stationary operation, and in that context it functioned very well. All other successful mobile SQUID systems are low temperature intrinsic gradiometers such as the Jena system in Germany. The exception to this is the new CSIRO high temperature intrinsic gradiometer system in Australia which is still in development and has not yet reached full-tensor capability. We believe that it is worthwhile to continue monitoring the activities of these groups. If it becomes likely that their systems have successfully overcome their hurdles then it would be worthwhile to conduct a demonstration of those systems for UXO surveying.

In reconsidering how to maximize the utility of the SQUIDs combination of high-sensitivity and full-tensor gradiometry from the numerous lessons learned in this project, we should recognize the limitations of that technology also. The SQUID does not reach its background noise level below 100Hz. For magnetic UXO detection the response bandwidth is typically DC-10Hz. In this range most sensors display a 1/f noise spectrum. The SQUID is also a relative sensing instrument, whereas most inversion routines require absolute field measurements. Finally, gradient calculation by subtracting independent components is more difficult than intrinsic gradient measurements. Combining these three factors, the ideal use of SQUID technology for UXO detection would appear to be a low temperature intrinsic gradiometer deployed as a TEM receiver. This would move the response bandwidth into a more favorable range, avoid the necessity of absolute field measurements and still provide full-tensor output. We believe that future work should concentrate on progressing towards that goal for this technology.

Bibilography

Blakely, R.J., 1996, Potential theory in gravity & magnetic applications: Cambridge University Press.

Bracken, R.E., Smith, D.V., Brown, P.J., 2004, Calibrating a tensor magnetic gradiometer using spin data: Society of Exploration Geophysics Annual Meeting Conference Proceedings, 4p.

Brown, P.J., Bracken, R.E., Smith, D.V., 2004, A case study of magnetic gradient tensor invariants applied to the UXO problem: Society of Exploration Geophysics Annual Meeting Conference Proceedings, 4p.

Clarke, J., 1994, SQUIDs: Scientific American, August 1994, p46-53.

Clem, T.R., Froelich, M.C., Overway, D.J., Purpura, J.W., Wiegert, R.F., Koch, R.H., Lathrop, D.K., Rozen, J., Eraker, J.H., Schmidt, J.M., 1997, Advances in sensor development and demonstration of superconducting gradiometers for mobile operation: IEEE Transactions on Applied Superconductivity, Vol. 7, No. 2, p3287-3293.

Clem, T.R., 1997, Naval Research Reviews, Vol. 69, No. 3, p29-45.

Foley, C.P., Leslie, K.E., Potential use of high Tc SQUID for airborne electromagnetics. Exploration Geophysics, Vol 29, p30-34.

Foley, C.P., Leslie, K.E., Binks, R., Lewis, C., Murray, W., Sloggett, G.J., Lam, S., Sankrithyan, B., Savvides, Katzaros, A., Muller, K.H., Mitchell, E.E., Pollock, J., Lee, J., Dart, L., Barrow, R.R., Asten, M., Maddever, A., Panjkovic, G., Downey, M., Hoffman, C., Turner, R., 1999, Field trials using HTS SQUID magnetometers for ground-based and airborne geophysical applications, IEEE Transactions on Applied Superconductivity, Vol. 9, No. 2, p3786-3792.

Foley, C.P., Tilbrook, D.L., Leslie, K.E., Binks, R.A., Donaldson, G.B., Du, J., Lam, S.K., Schmidt, P.W., Clark, D.A., 2001, Geophysical exploration using magnetic gradiometry based on HTS SQUIDs, IEEE Transactions on Applied Superconductivity, Vol. 11, No. 1, p1375-1378.

Gamey, T.J., Doll, W.E., Beard, L.P., Bell, D.T., 2004, Analysis of correlated noise in airborne magnetic gradients for UXO detection: Journal of Environmental and Engineering Geophysics, Vol 9, Issue 3, p115-126.

Heath, P., Heinson, G., Greenhalgh, S., 2003, Some comments on potential field tensor data: Exploration Geophysics, Vol. 34, p57-62.

Hoburg, J.F., 1995, Principles of quasistatic magnetic shielding with cylindrical and spherical shields, IEEE Transactions on electromagnetic compatibility, Vol. 37, No. 4, p574-579.

Jia, J., Lo, B., Groom, R., 2004, Final report on improved aeromagnetic compensation: OMET Program Report #P02-03-043, 70p.

Koch, R.H., 1997, Maximum theoretical bandwidth and slewrate of a DC SQUID feedback system: IEEE Transactions on Applied Superconductivity, Vol. 7, No. 2, p3259-3262.

Lee, J.B., Dart, D.L., Turner, R.J., Downey, M.A., Maddever, A., Panjkovic, G., Foley, C.P., Leslie, K.E., Binks, R., Lewis, C., Murray, W., 2002, Airborne TEM surveying with a SQUID magnetometer sensor: Geophysics, Vol. 67, No. 2, p468-477.

Nelson, J.B., 2002, Final report on the airborne superconducting quantum interference device (SQUID) magnetic gradiometer program, Defence R&D Canada, Technical Memorandum DREA TM 2001-126, 44p.

Nelson, J.B., 1988, Calculation of the magnetic gradient tensor from total field gradient measurements and its application to geophysical interpretation, Geophysics, Vol. 53, No. 7, p957-966.

Pedersen, L.B., Rasmussen, T.M., 1990, The gradient tensor of potential field anomalies: Some implications on data collection and data processing of maps: Geophysics, v. 55, 1558-1566.

Sarwinski, R.E., 1977, Superconducting instruments: Cryogenics, Dec. 1977, p671-679.

Schmidt, P., Clark, D., Leslie, K., Bick, M, Tilbrook, D., Foley, C., 2001, GETMAG – a new magnetic tensor gradiometer for exploration, 2004, Extended Abstract in the Proceedings of ASEG 17th Geophysical Conference and Exhibition, Syndey, 2004., 4p.

Varpula, T., Putanen, T., 1984, Magnetic field fluctuations arising from thermal motion of electric charge in conductors: Applied Physics, Vol. 55, No. 11, p4015-4021.

Wilson, H., 1985, Analysis of the magnetic gradient tensor: Defence Research Establishment Pacific, Canada Technical Memorandum, 85-13, 47p.

Wynn, W.M., 1995, Magnetic dipole localization using the gradient rate tensor measured by a five-axis magnetic gradiometer with known velocity, SPIE Vol. 2496, p357-367.

Wynn, W.M., Frahm, C.P., Carroll, P.J., Clark, R.H., Wellhoner, J., Wynn, M.J., 1975, Advanced superconducting gradiometer/magnetometer arrays and a novel signal processing technique: IEEE Transactions on Magnetics, vol. MAG-11, No. 2, p701-707.

Zhang, C., Mushayandebvu, M.F., Reid, A.B., Fairhead, J.D., Odegard, M.E., 2000, Euler deconvolution of gravity tensor gradient data: Geophysics, Vol. 65, No. 2, p512-520.